arXiv:2405.17294v2 [astro-ph.EP] 24 Jul 2024

Non-Detections of Helium in the Young Sub-Jovian Planets K2-100b, HD 63433b, & V1298 Tau c

Munazza K. Alam [ID],[1, 2, *] James Kirk [ID],[3, 4, *] Leonardo A. Dos Santos [ID],[1] Patrick McCreery [ID],[5]
Andrew P. Allan [ID],[6] James E. Owen [ID],[3] Aline A. Vidotto [ID],[6] Romain Allart [ID],[7] Vincent Bourrier [ID],[8]
Néstor Espinoza [ID],[1] George W. King [ID],[9] Mercedes López-Morales [ID],[4] and Julia V. Seidel [ID][10]

[1]Space Telescope Science Institute, 3700 San Martin Drive, Baltimore, MD 21218, USA
[2]Carnegie Earth & Planets Laboratory, 5241 Broad Branch Road NW, Washington, DC 20015, USA
[3]Department of Physics, Imperial College London, Prince Consort Road, London, SW7 2AZ, UK
[4]Center for Astrophysics | Harvard & Smithsonian, 60 Garden Street, Cambridge, MA 02138, USA
[5]William H. Miller III Department of Physics and Astronomy, Johns Hopkins University, Baltimore, MD 21218, USA
[6]Leiden Observatory, Leiden University, P.O. Box 9513, 2300 RA Leiden, The Netherlands
[7]Département de Physique, Institut Trottier de Recherche sur les Exoplanètes, Université de Montréal, Montréal, Québec, H3T 1J4,
Canada
[8]Observatoire Astronomique de l'Université de Genève, Chemin Pegasi 51b, CH-1290 Versoix, Switzerland
[9]Department of Astronomy, University of Michigan, Ann Arbor, MI 48109, USA
[10]European Southern Observatory, Alonso de Córdova 3107, Vitacura, Región Metropolitana, Chile

ABSTRACT

We search for excess in-transit absorption of neutral helium at 1.083 μm in the atmospheres of
the young (<800 Myr) sub-Jovian (0.2–0.5 R_J) planets HD 63433b, K2-100b, and V1298 Tau c using
high-resolution (R∼25,000) transit observations taken with Keck II/NIRSPEC. Our observations do
not show evidence of helium absorption for any of the planets in our sample. We calculate 3σ upper
limits on the planets' excess helium absorption of <0.47% for HD 63433b, <0.56% for K2-100b and
<1.13% for V1298 Tau c. In terms of equivalent width, we constrain these to <2.52, <4.44 and
<8.49 mÅ for HD 63433b, K2-100b and V1298 Tau c, respectively. We fit our transmission spectra
with one-dimensional Parker wind models to determine upper limits on the planets' mass-loss rates
of <7.9×10^{10}, <1.25×10^{11} and <7.9×10^{11} g s^{-1}. Our non-detections align with expectations from
one-dimensional hydrodynamic escape models, magnetic fields, and stellar wind confinement. The
upper limits we measure for these planets are consistent with predicted trends in system age and He
equivalent width from 1D hydrodynamic models.

1. INTRODUCTION

Short-period planets intermediate in size between
Earth and Neptune (1–4 $R_\oplus$), are abundant in the
galaxy (e.g., Batalha et al. 2013; Dressing & Charbon-
neau 2015; Morton et al. 2016), but their formation and
evolutionary histories are currently unknown. While
those larger than 1.6 $R_\oplus$ likely possess large H/He en-
velopes comprising ∼1% of their total mass, planets be-

Corresponding author: Munazza K. Alam & James Kirk
malam@stsci.edu, j.kirk22@imperial.ac.uk

* These authors contributed equally to this work.

low this threshold have densities consistent with rocky
compositions (e.g., Rogers 2015). The observed distri-
bution of transiting planetary radii from *Kepler* further
reveals a dearth of exoplanets with radii between 1.5–
2.0 $R_\oplus$ (Fulton et al. 2017). While planet formation and
core-powered evolution models can partly explain these
results (e.g., Ginzburg et al. 2018; Loyd et al. 2018),
photoevaporation – the escape of planetary atmospheres
caused by high-energy irradiation from their host stars –
may play an important role in sculpting these observed
trends (e.g., Lopez & Fortney 2014; Owen & Wu 2017).

Intermediate-sized planets are the best targets for
probing atmospheric escape that changes the bulk char-
acteristics of exoplanets. Jupiter-sized planets are too

massive to lose a significant part of their primordial atmospheres during their evolution (e.g., Lecavelier Des Etangs 2007), whereas small Earth-sized planets lose their volatile-rich atmospheres too quickly (e.g., Owen & Wu 2017) and are not accessible with currently-available instruments (e.g., Bourrier et al. 2017; Waalkes et al. 2019). Some of the most extreme cases of ongoing atmospheric escape and evolution have been observed for planets with sizes similar to Neptune: GJ 436b (Ehrenreich et al. 2015), GJ 3470b (Bourrier et al. 2018), HAT-P-11b (Allart et al. 2018; Mansfield et al. 2018; Ben-Jaffel et al. 2022), and tentatively K2-18b (Dos Santos et al. 2020). Signatures of atmospheric escape imprint large ($\sim$0.1–5% for He; $\gtrsim$10% for H) signals on transit spectra that are readily detectable with current instruments.

The majority of observations of atmospheric escape and extended atmospheres prior to 2018 were obtained with Lyman-α transmission spectroscopy using *Hubble* (e.g., Vidal-Madjar et al. 2003; Lecavelier Des Etangs et al. 2010; Ehrenreich et al. 2015; Bourrier et al. 2018; Dos Santos et al. 2020). The stellar Lyman-α emission line is efficiently absorbed by the interstellar medium (ISM), limiting the detection of atmospheric escape to nearby ($\lesssim$60 pc) targets. Spake et al. (2018), however, demonstrated that the metastable He triplet at 1.083 μm – which is devoid of ISM absorption – is a viable probe for atmospheric escape (Seager & Sasselov 2000; Oklopčić & Hirata 2018). Several studies have since demonstrated the feasibility of ground-based transmission spectroscopy to study atmospheric escape via the 1.083 μm He triplet (e.g., Allart et al. 2018; Nortmann et al. 2018; Alonso-Floriano et al. 2019; Kirk et al. 2020; Zhang et al. 2021). Kirk et al. (2020) showed for the first time the capability of Keck II/NIRSPEC to achieve high-precision, high-confidence (30σ) detections of excess He absorption.

Photoevaporation models predict that planets lose a significant amount of their primordial H/He atmospheres at early ages ($\tau <$ 100-500 Myr) when high-energy irradiation from the host star is the strongest (e.g., Jackson et al. 2012; Owen & Wu 2013). Detecting and measuring the atmospheric escape rates from young planets can allow us to place more direct observational constraints on planetary evolution models at early ages. These young targets are further favorable for helium observations because the intense stellar X-ray and extreme ultraviolet (XUV) irradiation levels in the first 100 Myr of a planet's lifetime lead to a metastable He line that is more likely to be populated (Oklopčić 2019; Allan et al. 2024). Young transiting planets thereby represent an

unprecedented opportunity to probe atmospheric escape and evolution in small, irradiated planets.

In this work, we present high-resolution spectroscopic observations of He I at 1.083 μm using Keck II/NIRSPEC in the young ($<$800 Myr) sub-Jovian (0.2–0.5 R_J) planets K2-100b (Livingston et al. 2018), HD 63433b (Mann et al. 2020), and V1298 Tau c (David et al. 2019) to measure the persistence and amplitude of the helium feature in young planets. The system and orbital properties of our sample are included in Table 1. While photoevaporation is predicted to be most significant at the earliest ages ($<$500 Myr; Lopez et al. 2012; Owen & Wu 2013), there are few observational tests of this theory and a lack of planets sampling the upper limit of this theoretical age limit. Therefore, our sample spans ages where photoevaporation should be dominant (23 Myr) up to ages older than we would expect photoevaporation to be dominant (750 Myr), enabling important tests of this theory.

The paper is structured as follows. §2 details the observations and data reduction procedures, and §3 describes our time-series analysis to obtain the helium transmission spectra for the planets in our sample. We interpret our observations considering the effects of magnetic fields, stellar winds, and 1D hydrodynamic escape models in §4. In §5, we contextualize our results in light of previous observations of these targets as well as other helium observations for both young and older exoplanets. We summarize our conclusions in §6.

2. OBSERVATIONS & DATA REDUCTION

2.1. *Observations*

We observed a single transit each of V1298 Tau c, HD 63433b, and K2-100b with Keck II/NIRSPEC (McLean et al. 1998; Martin et al. 2018) on UT 17 Dec 2020, UT 24 Dec 2020, and UT 08 Jan 2021, respectively. Our observations were taken as part of Program N165 (PI: Alam) using the NIRSPEC-1 filter, which covers the Y-band (0.947–1.121 μm; NIRSPEC orders 68-80) at a spectral resolution of R$\sim$25,000. Here we present the extracted NIRSPEC order 70 (1.0799–1.1014 μm) spectra only, which covers the metastable helium triplet at 1.0833 μm.

To mitigate fringing effects, we did not use the 'Thin' blocking filter (e.g., Kasper et al. 2020; Kirk et al. 2022). At the beginning and end of our transit observations, we obtained a set of 11 darks (including bias frames), 11 lamp flats, and two arcs (each composed of 10 coadded Ne, Ar, Xe, and Kr arc lamps). We obtained 28 spectra for V1298 Tau c (J=8.6) with exposure times of

Table 1. System Parameters for HD 63433b, V1298 Tau c, & K2-100 b. Integrated fluxes received by each planet over the X-ray [0.517-12.4 nm], hard-EUV [10-36 nm], soft-EUV [36-92 nm] and mid-UV [91.2-320 nm] bands from the Allan et al. (2024) model. Stellar, planetary, and system parameters are taken from (a) Mann et al. (2020), (b) Capistrant et al. (2024), (c) Jones et al. (2015), (d) Gaia DR2, (e) Barragán et al. (2019), (f) Brandt & Huang (2015), (g) David et al. (2019), (h) Gaidos et al. (2022), (i) derived from mass-radius relation (Chen & Kipping 2017), (j) Stassun et al. (2019).

	HD 63433b	V1298 Tau c	K2-100 b
Stellar Parameters			
Mass, $M_\star$ [M$_\odot$]	0.99 ± 0.03^a	1.10 ± 0.05^g	1.15 ± 0.05^e
Radius, $R_\star$ [R$_\odot$]	0.91 ± 0.03^a	1.34 ± 0.05^g	1.24 ± 0.05^e
Effective temperature, $T_{\rm eff}$ [K]	5640 ± 74^a	$4962^{+88}_{-45}\,^d$	5945 ± 110^e
Metallicity, [Fe/H]	0.03 ± 0.05^b	0.139 ± 0.03^j	0.22 ± 0.09^e
Surface gravity, log(g) [cgs]	4.52 ± 0.05^b	4.25 ± 0.03^g	4.33 ± 0.10^e
Age [Myr]	414 ± 23^c	23 ± 4^g	750 ± 5^f
$F_{\rm X-ray}$ [erg/s/cm^2]	5.39×10^3	1.84×10^5	1.98×10^4
$F_{\rm hEUV}$ [erg/s/cm^2]	4.64×10^3	3.75×10^4	1.70×10^4
$F_{\rm sEUV}$ [erg/s/cm^2]	6.75×10^3	1.73×10^4	4.60×10^4
$F_{\rm mid-UV}$ [erg/s/cm^2]	5.33×10^6	1.19×10^6	3.21×10^6
Planetary Parameters			
Mass, M_p [M$_{\rm J}$]	0.0166^i	0.0839^i	0.0686 ± 0.02^e
Radius, R_p [R$_{\rm J}$]	0.192 ± 0.009^a	0.499 ± 0.03^g	0.346 ± 0.01^e
Equilibrium temperature, T_{eq} [K]	968 ± 36^a	981 ± 31^g	1841 ± 41^e
Surface gravity, log(g) [cgs]	3.05^i	2.92^i	3.15 ± 0.13^e
System Parameters			
Systemic velocity, γ [km/s]	-16.31 ± 0.20^d	$+14.644\pm0.136^h$	$+34.78\pm0.64^d$
Period, P [days]	7.10793 ± 0.0004^a	8.24958 ± 0.00072^g	1.6739035 ± 0.0000004^e
Inclination, i [°]	$89.38^{+0.43}_{-0.64}\,^a$	$88.49^{+092}_{-0.72}\,^g$	81.27 ± 0.37^e
Scaled semi-major axis, $a/R_\star$	$16.95^{+0.34}_{-0.82}\,^a$	13.19 ± 0.55^g	5.21 ± 0.13^e
Radius ratio, $R_p/R_\star$	0.02161 ± 0.00055^a	0.0381 ± 0.0017^g	0.02867 ± 0.00028^e
Mid-transit time, T_0 [BJD]	$2458916.4526^{+0.0032}_{-0.0027}\,^a$	2457064.2797 ± 0.0034^g	$2457140.71941\pm0.00027^e$
Transit duration [days]	0.134 ± 0.0014^a	0.194 ± 0.005^g	0.067 ± 0.0006^e

300 seconds each over 182 minutes, and acquired an additional 6 out-of-transit spectra for this target on UT 08 Jan 2021[1]. For HD 63433b (J=5.6), we acquired 372 spectra with exposure times of 30 seconds over the course of 303 minutes. For K2-100b (J=9.4), we obtained 26 600-second spectra over 255 minutes. For all of our observations, we used an ABBA nod pattern to remove sky background by A-B pair subtraction. We achieved an average SNR per pixel per exposure in or-

der 70 of 199, 213, and 191 for V1298 Tau c, HD 63433b, and K2-100b, respectively.

2.2. *Data Reduction*

We reduced our observations using the REDSPEC[2] software (McLean et al. 2003, 2007), which performs spatial rectification of tilted spectral orders on the detector, bad pixel interpolation, flat-fielding, and dark and bias subtraction. For the dark subtraction and flat-field correction steps in REDSPEC, we created a main dark and a main flat by median-combining our 22 darks and 22

---

[1] The first night of V1298 Tau data was severely affected by bad weather, limiting the number of out-of-transit exposures to 3.

[2] https://www2.keck.hawaii.edu/inst/nirspec/redspec.html

flats, respectively. We used a second-order polynomial to correct for the tilt of the spectral orders on the detector. We then performed a wavelength calibration for order 70 using our arc lamp spectra and a second-order polynomial to map the measured arc line locations to the theoretical values. The spectra were then extracted in differenced A-B nod pairs to remove the sky background and OH emission lines, with an aperture width of 11 pixels.

2.3. *Post-Processing*

We post-processed the extracted stellar spectra following the prescription outlined in Kirk et al. (2022), which we briefly summarize here. After extracting the wavelength-calibrated time-series spectra, we continuum-normalized the spectra using iSpec[3] (Blanco-Cuaresma et al. 2014; Blanco-Cuaresma 2019). We fit cubic splines to the 1.080-1.095 μm portion of order 70, masking the helium triplet from our continuum calculation.

We then used molecfit[4] (Kausch et al. 2015; Smette et al. 2015) to remove telluric features. We selected telluric absorption lines away from stellar absorption lines to constrain the molecfit model, fitting for atmospheric H_2O only. For HD 63433b, we used seven telluric absorption lines and three for K2-100b. For V1298 Tau c, we used four telluric absorption lines for the December observations and three for the January observations. We fitted the telluric absorption lines with a Gaussian with a FWHM initiated at 3.5 pixels. The FWHM of the Gaussian was fixed to 3.5 pixels for K2-100b following (Zhang et al. 2021; Kirk et al. 2022), due to difficulties in the ability of the data to constrain this parameter for this night. The fitted FWHMs of the telluric models for the other two targets were 3.33 ± 0.16 pixels (HD 63433b) and 3.73 ± 0.26 pixels (V1298 Tau c). Example telluric-corrected spectra are shown in Figure 1.

To check our systematic errors in the wavelength solution near the He triplet, we cross-correlated our stellar spectra with model spectra that combined PHOENIX stellar atmosphere models (Husser et al. 2013) with a telluric model from the molecfit[5] software (Kausch et al. 2015; Smette et al. 2015). By cross-correlating sub-sections of the spectral order, we found that the bluest wavelengths ($\leq 1.087\,\mu$m) were shifted from the truth by $\sim$30 km s^{-1} for K2-100b, $\sim$12 km s^{-1} for HD 63433b and $\sim$-10 km s^{-1} for V1298 Tau c. However, at the reddest wavelengths ($\geq 1.092\,\mu$m) the spectra
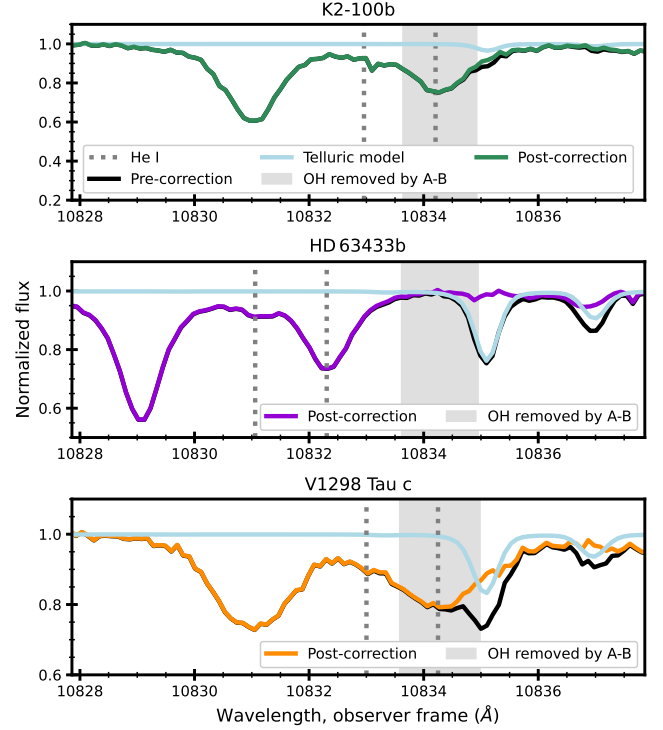
Figure 1. Examples of pre- (black) and post-telluric corrected spectra for K2-100b (green), HD 63433b (purple), and V1298 Tau c (orange). The best-fitting molecfit H_2O models are shown in light blue. The telluric OH emission occurs in the shaded gray region, however, this feature is successfully removed by the A-B nod pair subtraction. The dashed gray lines indicate the location of the He triplet which are different in the observer frame due to the combination of the barycentric and systemic velocities.

were shifted by -2 km s^{-1}, -5 km s^{-1} and 1 km s^{-1}, respectively. We corrected for this wavelength distortion by fitting a quadratic polynomial to our wavelength-dependent cross-correlation results. As a final check to our wavelength solution, we fit a Voigt absorption profile to a non-saturated absorption line at 1.0842 μm in the same spectral order and measured the center of the fitted profile for each exposure. We then calculated its shift in Doppler velocity space from the average stellar spectrum, and correct the wavelength solution in the He triplet region based on this systematic Doppler velocity shift; this procedure was repeated for each exposure.

We then shifted all of the spectra from the observer rest frame to the stellar rest frame by correcting for the barycentric, systemic, and stellar reflex velocities (Wright & Eastman 2014). To account for cosmic rays in our datasets, we constructed a median-combined spectrum and compared each spectral frame to the combined spectrum. We replaced data points that deviated by $>4\sigma$ from the median spectrum to the median of the sur-

rounding pixels. We flagged 11 outliers for HD 63433b and 14 outliers for V1298 Tau c within ±20 km/s of the helium triplet in the planets' rest frames but opted not to replace these to avoid removing real planetary signal. Due to the larger amplitude and greater number of outliers in the K2-100 data set (26 pixels within ±20 km/s of the helium triplet, equal to 5% of the total pixels) we replaced these to avoid anomalous signals caused by outliers.

3. TIME-SERIES ANALYSIS

We first generated the mean in-transit and out-of-transit spectra in order to determine the in-transit excess absorption signal. We constructed the in-transit spectrum by computing the weighted mean (weighted by the spectral uncertainties) of spectra taken between the second and third contact points; the out-of-transit spectrum was constructed by computing the weighted mean of the spectra taken before first contact and after fourth contact. To determine the contact points, we used the ephemerides of V1298 Tau c, HD 63433b, and K2-100b from David et al. (2019), Mann et al. (2020), and Barragán et al. (2019), respectively. The individual order 70 spectra, as well as the mean in- and out-of-transit spectra, for the planets in our sample are shown in Figures 2, 3, and 4. We find that there is no apparent excess absorption centered on the helium triplet for any of the planets in our sample. We also constructed phase-resolved maps centered on the helium line in our search for excess absorption around 1.083 μm, computed by dividing each spectrum of the time-series by the mean out-of-transit spectrum. The phase-resolved excess absorption maps are shown in Figures 5, 6, and 7.

We then constructed the helium transmission spectra for K2-100b, HD 63433b, and V1298 Tau c, by shifting the excess absorption to each planet's respective rest frame, which are shown in Figure 8. Since the native uncertainties in the transmission spectra are not representative of the scatter in the data due to the presence of correlated noise, we inflated our uncertainties to account for the actual scatter in the data. This step was necessary as, without it, we could infer anomalous or overly precise measurements of planetary absorption. We do this by setting the uncertainties in the helium transmission spectra to be equal to the standard deviation of the transmission spectra. From our spectra, we place 3σ upper limits on the excess He absorption of 0.56% for K2-100b, 0.47% for HD 63433b and 1.13% for V1298 Tau c. These upper limits are equal to three times the standard deviation of the (flat) transmission spectra taken from ±10 Å around the He triplet. We also calculate upper limits on the equivalent width (EW) by integrating

the transmission spectra between 10831–10835 Å. This leads to upper limits on the EW of <4.44 mÅ for K2-100b, <2.52 mÅ for HD 63433b and <8.49 mÅ for V1298 Tau c. From both the mean in-transit and out-of-transit spectra as well as the excess absorption maps, we do not identify excess absorption for the planets in our sample. We use the p-winds (Dos Santos et al. 2022) code to place upper limits on the in-transit He absorption (§4.2).

4. HELIUM NON-DETECTIONS IN CONTEXT

We consider our non-detections of excess helium absorption in light of the effects of stellar winds and magnetic fields on depopulating the metastable helium line (§4.1), 1D isothermal escape models (Parker winds; §4.2), and photoevaporation-driven hydrodynamic escape models (§4.3).

4.1. *Stellar Winds & Magnetic Fields*

Given our non-detections, we should assess whether they agree with the basic predictions of outflow models. A hydrodynamically launched outflow can only be accelerated up to trans-sonic velocities. Beyond the sonic regime, the velocity remains approximately constant (e.g., Lammer 2013) and the density profile falls off as $1/r^2$. When the helium triplet state is depopulated by electron collisions (rather than photoionizations), as is expected for K-stars (Oklopčić 2019), the helium triplet fraction is roughly constant at large radius. This means that the helium absorption is dominated by the contribution from large radius, rather than close to the planet. Therefore, the helium absorption signal is dominated by how far the outflow extends spherically away from the planet. In the case of limited stellar wind, the outflow can ultimately only remain spherical out to the Hill sphere; whereas a strong stellar wind can crush the planetary outflow to a fraction of its Hill sphere (Carolan et al. 2020). Given a maximum radius out to which the outflow remains spherical ($R_{\rm out}$), the maximum possible excess absorption is:

$$\approx \left[1 - \left(\frac{R_p}{R_{\rm out}}\right)^2\right] \left(\frac{R_{\rm out}}{R_*}\right)^2 \qquad (1)$$

in the case that the outflow is optically thick in transmission at $R_{\rm out}$. Setting $R_{\rm out}$ to the Hill sphere radius $R_{\rm H}$ yields maximum excess optical depths of 1.9%, 8.4%, and 4.7% for K2-100b, HD 63433b, and V1298 Tau c, respectively. The fact that these maximal excess depths are only a factor of ~4 larger than our upper limits for K2-100b and V1298 Tau c implies that a transmission optical depth in helium of $\lesssim 0.25$ would be sufficient to render the helium absorption below our detection limit. Thus, since the helium line is normally optically thin,

these non-detections are not surprising. For an optically thin $1/r^2$ density profile, the excess absorption becomes:

$$\approx 2\sigma_{\mathrm{He3}}\pi n_{He3}(R_{\mathrm{out}})R_{\mathrm{out}} \left(1 - \frac{R_p}{R_{\mathrm{out}}}\right)\left(\frac{R_{\mathrm{out}}}{R_*}\right)^2 \quad (2)$$

where σ_{He3} is the cross-section at $10830\,\text{Å}$ (appropriately averaged over our R$\sim$25,000 spectral resolution) and $n_{He3}(R_{\mathrm{out}})$ is the density of metastable helium at R_{out}. Even with the optimistic assumption that all helium is neutral and an extreme helium triplet fraction of 10^{-5}, for a Solar ratio of hydrogen to helium the excess helium absorption remains below our upper limits for K2-100b and V1298 Tau c with mass-loss rates up to 10^{11} and 3×10^{11} g s^{-1}, respectively. These limits are consistent with typical energy-limited mass-loss rates.

Applying the same methodology to HD 63433b would require a mass-loss rate below 10^{10} g s^{-1} due to its larger Hill sphere – but this estimate is in tension with model expectations, of several 10^{10} g s^{-1}. One immediate solution would be to reduce the outer radial extent of the outflow by its interaction with the stellar wind. To crush the planetary outflow to a sufficiently small size to be consistent with our non-detection would require a stellar wind with a velocity at the planet of several hundred km s^{-1} to have an outflow rate of $\sim$10^{-12} M$_\odot$ yr^{-1}, approximately a hundred times larger than that of the Sun. Given the young age of the HD 63433 system and its observed X-ray properties, such a large stellar wind outflow rate is consistent with empirical scaling relationships (e.g. Wood et al. 2005; Johnstone et al. 2015; Blackman & Owen 2016). We note that a study using Zeeman-Doppler Imaging infers stellar mass-loss rates in the range $1-4\times10^{-13}$ M$_\odot$ yr^{-1} (Bellotti et al. 2024).

An alternative explanation for HD 63433b is the presence of a strong planetary magnetic field. Schreyer et al. (2023) demonstrated that any planetary magnetic field can suppress the helium transmission signal. This arises from two interrelated effects. Firstly, since the majority of the gas is confined by closed planetary magnetic fields, it cannot expand and cool as a result of stellar XUV heating. Thus, the gas is heated to $\sim$10^4 K where Lyman-α cooling becomes efficient, thermostating the gas at $\sim$10^4 K (e.g., Murray-Clay et al. 2009; Owen & Wu 2016). Around K-stars, the helium triplet state is depopulated by collisions with electrons (Oklopčić 2019) and populated by recombinations – processes that both happen less efficiently at high temperatures, resulting in a significantly lower population of metastable helium (Biassoni et al. 2023).

Secondly, the outflowing regions near the pole have lower densities than a spherically symmetric outflow. This is because the outflow – forced to follow planetary

magnetic field lines – has a streamline divergence that falls faster than $1/r^2$. In the outflow regions near the pole, the streamline divergence falls off as $1/r^3$ (Adams 2011; Owen & Adams 2014). This difference is important because for a $1/r^2$ density profile the helium absorption signal is dominated by absorption far from the planet, where it covers a larger area of the star (Equation 2); whereas for $1/r^3$ the absorption is more weighted toward the regions closer to the planet where they cover less of the star's area. As Schreyer et al. (2023) demonstrated, this effect significantly reduces the helium absorption for a planet with a strong magnetic field, where the excess absorption for a $1/r^3$, compared to a $1/r^2$ density profile is of order R_p/R_{out} smaller, which is $\sim$0.1 for HD 63433b. As discussed by Zhang et al. (2022b), planetary magnetic fields could be responsible for the He non-detection. Following the methodology in Owen & Adams (2014), we estimate a surface dipole planetary magnetic field strength of $\sim$4-5 G to close >50% of the planetary field lines.

4.2. Parker Wind Models

We modeled the helium transmission spectra presented in §3 for HD 63433b, K2-100b, and V1298 Tau c using the one-dimensional atmospheric escape model p-winds[6] (Dos Santos et al. 2022; Dos Santos & Vissapragada 2023). This open-source Python-based code is based on the framework of Oklopčić & Hirata (2018) and Lampón et al. (2020), and has been benchmarked against the EVaporating Exoplanets (EVE) code (Bourrier & Lecavelier des Etangs 2013; Bourrier et al. 2015). The model treats the escaping material as an isothermal Parker wind (Parker 1958) composed only of hydrogen and helium, finds the steady-state recombination/ionization solutions for the distribution of neutral hydrogen and helium in the planetary upper atmosphere, and solves the radiative transfer equation to determine the in-transit absorption due to the escaping planetary material. The p-winds code requires as input high-energy spectral energy distributions (SEDs) of the host stars HD 63433, K2-100, and V1298 Tau. The SEDs of V1298 Tau and HD 63433 that we use are adapted from Duvvuri et al. (2023) and Zhang et al. (2022c), respectively. For K2-100, since there is no archival high-energy spectrum available, we adopted the SED of the similarly young (600 Myr) and solar-type star ι Horologii (Sanz-Forcada et al. 2019) scaled to the system's stellar radius and semi-major axis. For these models, we assume that the outflow is composed solely of H and He,

---

[6] https://github.com/ladsantos/p-winds

and that H/He ratio is 90/10 in number of particles. We adopt the stellar and planetary parameters in Table 1.

Correlated noise is prevalent in the excess absorption spectra shown in Figure 8. Potential sources of correlated noise in the data may be instrumental or astrophysical in origin, including not limited to telluric contamination, wavelength calibration, stellar activity, and temporal variability in the the deep Mg 10811 Å, Si 10827 Å, and Si 10844 Å lines (e.g., Guilluy et al. 2023; Zhang et al. 2023; Vissapragada et al. 2024). Therefore, we model the excess absorption spectra as a planetary absorption combined with correlated noise. To accurately constrain the mass loss, outflow temperature, and outflow velocity, we employ the use of Gaussian processes (GPs) to account for systematic uncertainties and model the correlated noise (Rasmussen & Williams 2006). The Matérn-3/2 kernel is used as the covariance function for the GPs, allowing for smoothness in our correlated noise functions (Foreman-Mackey et al. 2017). Gaussian processes allow for the fitting of the true helium absorption signal, removing the correlated noise present in the data. The use of Gaussian processes introduces two parameters (the systematics amplitude σ and length scale ρ), which, when paired with the three p-winds parameters (mass-loss rate, outflow temperature, and outflow radial velocity), creates a five-dimensional model. The systematics and planetary absorption are fitted simultaneously. The Bayesian inference we designed avoids overfitting by applying a prior for the GP parameters inferred from the transmission spectrum outside of the He feature. This methodology will be discussed in more detail in an upcoming paper (McCreery et al., in prep.). When constraining the posteriors of these five parameters given the transmission spectra, we use nested sampling (Speagle 2020). Nested sampling is advantageous over Monte Carlo methods in this situation due to our poor prior information and nested sampling's ability to estimate the marginal likelihood, which aids in model selection.

In summary, our model uses nested sampling to perform fits of the helium absorption spectrum of HD 63433b, K2-100b, and V1298 Tau c using p-winds to fit for the helium signature and Gaussian processes to account for correlated noise. The resulting best-fit systematics and planetary signals are shown in Figure 9. We found that the nested sampling results favor a non-detection for HD 63433b with more than 95% confidence, a tentative detection at high blue-shifted velocities (-17 km s^{-1}) for K2-100b, and a marginal detection at high red-shifted velocities (+21 km s^{-1}) for V1298 Tau c. To confirm that our model is not overfitting the data, we also ran fits only including the

	K2-100b	V1298 Tau c	HD 63433b
$\log z_{\rm GP}$	461.17	392.43	490.59
$\log z_{\rm GP\, +\, p\text{-}winds}$	464.53	391.57	489.17
$|\Delta \log z|, |\log B_m|$	3.36	.85	1.42
p-value	.03	.70	.81

Table 2. Model comparisons between the Gaussian Process-only models and the full Gaussian Process + p-winds models using log-evidence ($\log z$). The Bayes factor, B_m, indicates that there are no significant differences in the model fits to the transmission spectra for V1298 Tau c and TOI-1726b. For K2-100b, however, the GP + p-winds model is moderately favored over the GP-only model.

GP component. Table 2 compares the results for the p-winds+GP models to GP only models. We find similar posterior distributions from this exercise compared to the p-winds+GP fits for V1298 Tau c and HD 63433b. For K2-100b, the p-winds+GP models are favored at the $\sim 3\sigma$ level because – although the length-scale of the GP is similar to the p-winds feature, the amplitude is clearly larger at the location of the He line.

Most detections of helium outflows in transiting exoplanets have been found to exhibit blue-shifted velocities up to ~ -10 km s^{-1} (McCreery et al., in prep.), a result that is theoretically expected for confined winds (MacLeod & Oklopčić 2022; Nail et al. 2023). Slightly red-shifted helium signals are expected for outflows in magnetized exoplanets (Schreyer et al. 2023). The outflow velocities measured by the nested sampling have never been observed before, are not predicted by state-of-the-art hydrodynamic escape models, and are likely spurious signals. The posterior distributions of the retrieved parameters from our p-winds modeling are shown in Table 3 and Figures 10, 11, and 12.

4.3. Photoevaporation-driven Hydrodynamic H/He Models

Additionally, we modeled HD 63433b, K2-100b, and V1298 Tau c using the one-dimensional hydrodynamic model described in Allan et al. (2024). This model self-consistently solves the hydrodynamic equations of atmospheric escape simultaneously with equations tracking the state of hydrogen, as well as helium in its 1^1S, 2^1S, 2^3S, singly and doubly ionized states. It considers the following hydrogen and helium processes: recombination, radiative decay, charge exchange between hydrogen and helium particles, collisional excitation, collisional ionization and photoionization. Fluxes in specified X-ray, soft and hard EUV, and mid-UV wavelength bins (see Table 1) are required as input in order to model photoionizations. To this end, we use the same SEDs described in §4.2. Table 1 lists the resulting band in-

Table 3. Parker-wind model constraints estimated for the observed transmission spectra

Planet	Excess Absorption	$\log \dot{m}$ (g s^{-1})	T ($\times 10^3$ K)	v (km s^{-1})
HD 63433b	<2.52 mÅ	< 10.9 (95% conf.)	> 5000 (prior)	No constraint
V1298 Tau c	<8.49 mÅ	< 11.9 (95% conf.)	> 5000 (prior)	$+21^{+23}_{-50}$
K2-100b	<4.44 mÅ	$11.10^{+0.23}_{-0.22}$	$7.2^{+2.3}_{-1.5}$	$-17.0^{+3.0}_{-2.0}$

tegrated fluxes adopted in our modeling. Having modeled the hydrodynamics, we then utilize the ray tracing model also described in Allan et al. (2024) to perform helium triplet transmission spectroscopy.

Predicted helium triplet absorptions for our three planets using the Allan et al. (2024) model are shown on the left-hand side of Figure 13. The models have been convolved to the spectral resolution (R∼25,000) of our observations. The solid lines show the mean average of phases between the transit's first and fourth points of contact, while the shaded region encompasses all phases between first-contact and mid-transit. The right-hand side of Figure 13 displays each planet's helium triplet extinction map across the stellar disk, as marked by the dashed circle. The displayed extinction is the sum of the individual extinction of each of the three lines of the triplet.

Despite assuming a large helium to hydrogen number fraction of He/H=0.1, the model predicts very weak absorption ($<0.05\%$) for HD 63433b, in agreement with the observations presented in Section §3. Its low mass-loss rate prediction of 2.8×10^{10} g s^{-1} is responsible for its low density and ultimately its weak helium triplet extinction, relative to the other planets.

The model for V1298 Tau c predicts a larger absorption more in line with the literature's current sample of detections with a mean predicted excess of 0.6% assuming He/H=0.1, although we note that this prediction is still below the upper limit of 1.13% we set from our observations. The predicted excess drops to 0.2% if we instead assume He/H=0.02 in the hydrodynamic model, as shown by the gray dashed line. Accordingly, re-observing V1298 Tau c with tighter uncertainties could help constrain the fraction of helium in this planet's atmosphere. Of the three planets, we predict V1298 Tau c to have the highest mass-loss rate, 2.2×10^{11} g s^{-1}. The greater atmospheric escape rate is due to a favorable combination of high EUV flux and low surface gravity (Allan & Vidotto 2019). The large escape rate, combined with a mid-UV flux sufficiently low so as to prevent significant depopulation of helium triplet by mid-UV photoionization, are responsible for its greater He transit absorption predicted in our modeling.

The predicted phase averaged excess absorption for K2-100b is ∼0.15%, also below the 3σ upper limit of 0.56% we get from the observation. Despite the low excess absorption, a large mass-loss rate of 1.1×10^{11} g s^{-1} is predicted by the model. The right-hand side of Figure 13 reveals that the weak absorption is partially due to its large impact parameter of $0.79 R_\star$.

5. DISCUSSION

5.1. *Comparison to Previous Observations*

5.1.1. *K2-100b*

High-resolution short-cadence spectroscopy from Subaru/IRD for K2-100b (Gaidos et al. 2020) yielded an upper limit on the planet's helium absorption of 5.7 mÅ in equivalent width and mass loss of 5.7×10^{10} g s^{-1} ($0.3 M_\oplus \, \mathrm{Gyr}^{-1}$) using a Parker wind model with temperatures below 10^4 K. With the Keck II/NIRSPEC data presented in this work, we can place tighter upper limits of <4.44 mÅ (0.56%) excess helium absorption. From our He transmission spectrum, we measure a mass-loss rate of 1.25×10^{11} g s^{-1} from our Parker wind models (see §4.2), which is ∼5× higher than that of Gaidos et al. (2020) and consistent with the §4.3 models. However, as we discussed in §4.2, our 1D Parker wind models for K2-100b converge to fit a likely spurious bump in our transmission spectrum and therefore our mass-loss measurements from this model are unreliable. Our theoretical 1D hydrodynamic models (§4.3) predict a mass-loss rate of 1.1×10^{11} g s^{-1}, which would correspond to He absorption of 0.15% and is below our detection threshold (0.56%). Gaidos et al. (2020) have a tighter upper limit on the mass-loss than we obtain from our 1D hydrodynamic models, despite having a looser upper limit on the helium equivalent width. This suggests that the differences in the mass-loss predictions from their study and ours may originate from the different model flux inputs, which would influence the resulting inferred transit absorptions.

5.1.2. *HD 63433b*

Previous Keck II/NIRSPEC observations of the HD 63433 system (Zhang et al. 2022c) placed an upper limit on HD 63433b's helium absorption of 0.5%, which is consistent with the 0.47% upper limit that we derive in this work. Zhang et al. (2022c) also noted that the stellar helium line varied during their transit observations, demonstrated by a darkening in the helium absorption map during the transit of HD 63433b. This darkening matches what we see in the data presented here (Fig-

ure 6), and induces an apparent helium *emission* feature (negative excess absorption) in the planet's transmission spectrum (Figure 8). Similar to Zhang et al. (2022c), we attribute this apparent emission to a darkening in the stellar helium triplet that is unrelated to the planet's atmosphere, suggesting that the stellar helium triplet is variable over the timescale of a transit observation. Zhang et al. (2022c) observed HD 63433b on 2021 January 7, two weeks after our observations. If this variability was to be seen in further subsequent epochs to have a period commensurate with the planet's orbital period, this could point to star-planet interactions, as has been proposed to explain the observed variation in the helium triplet for AU Mic (Klein et al. 2022a).

Using 3D hydrodynamic mass-loss models, Zhang et al. (2022c) compute a mass-loss rate of $6.6 \times 10^{10}\,\mathrm{g\,s^{-1}}$ ($0.35\,M_\oplus\,\mathrm{Gyr^{-1}}$) for HD 63433b, which implies a mass-loss timescale of 80 Myr. This timescale is consistent with the 95th percentile upper limit on the mass loss rate of $7.9 \times 10^{10}\,\mathrm{g\,s^{-1}}$ ($0.42\,M_\oplus\,\mathrm{Gyr^{-1}}$) derived from our Parker wind models, but higher than the rate $2.8 \times 10^{10}\,\mathrm{g\,s^{-1}}$ ($0.15\,M_\oplus\,\mathrm{Gyr^{-1}}$) inferred from our self-consistent hydrodynamic models (§4.2 and 4.3), respectively. Given the age of HD 63433b (414 ± 23 Myr; Mann et al. 2020), our `p-winds` and self-consistent model findings agree with Zhang et al. (2022c) in demonstrating that it is unlikely that the planet has retained a H/He atmosphere.

Our 1D hydrodynamic modeling yields a mass-loss rate that is ∼2.3 times smaller than the Zhang et al. (2022c) estimates, which consequently results in a smaller overall estimated outflow density. Although our model uses the same high-energy stellar SED as Zhang et al. (2022c), their model differs from ours in their treatment of the heating/cooling processes of the atmosphere. They also include the interaction with a stellar wind, but we believe the former difference is the likely cause of our differing evaporation rates. Because of the smaller escape rates and densities of our spherically symmetric models, it is expected that our excess helium absorption would differ from theirs: in fact, our excess helium absorption at the line center ($<0.05\%$) is an order of magnitude smaller than the model from Zhang et al. (2022c) for HD 63433b.

5.1.3. *V1298 Tau c*

Vissapragada et al. (2021) used narrowband photometry from Palomar/WIRC to search for helium in V1298 Tau c, but were unable to detect the planet's transit likely due to correlated noise in the data. Their non-detection is consistent with our findings for this planet (Figure 8), however, our upper limit on the ex-

cess helium absorption of 1.13% (EW < 8.49 mÅ) is the first quantitative upper limit for this planet. We checked whether our result was sensitive to our choice of ephemeris by re-doing our analysis with the ephemeris of Feinstein et al. (2022) and found a consistent upper limit to when we used the ephemeris from David et al. (2019). High-resolution optical spectra from GRACES on Gemini-North (Feinstein et al. 2021) revealed a tomographic signal in the Ca II triplet attributed to possible star-planet interactions, as well as excess Hα absorption smoothly decreasing during the planet's transit that can be explained by starspots and faculae rotating into and out of view.

Since the Ca II triplet arises in the chromosphere, searching for variability in other chromospheric lines may corroborate the star-planet interactions hypothesis (Feinstein et al. 2021). Given that the helium triplet is also a chromospheric line, we can search for variability in this line (Klein et al. 2022b). However, the variability we see in the stellar helium line, combined with the poor weather conditions during our observations, prevents us from testing the possibility of star-planet interactions.

Variability in V1298 Tau's stellar helium line has been seen on a number of previous occasions (e.g., Vissapragada et al. 2021; Gaidos et al. 2022; Krolikowski et al. 2024). Vissapragada et al. (2021) measured a difference in the stellar helium equivalent width of 0.15 Å over a two month timescale in addition to a flare in the helium line during a transit of V1298 Tau c. Gaidos et al. (2022) found a 50 % variability in the stellar helium line during a transit observation V1298 Tau b. In this case, the variability is neither due to stellar variability due to the short time scale involved, nor planet variability given the orbital phases at which this absorption is seen. Gaidos et al. (2022) instead suggest that the absorption they see could be associated with a transit of V1298 Tau d, which would be consistent with Vissapragada et al. (2021). We rule out seeing variability in the stellar He line at the amplitudes and timescales that Gaidos et al. (2022) see, reinforcing the conclusion that they were seeing absorption from V1298 Tau d.

V1298 Tau was also observed as part of Krolikowski et al. (2024)'s program to monitor the stellar He equivalent width of exoplanet host stars. For V1298 Tau, the youngest star in their sample, they observed variability in the He equivalent width with a median absolute deviation of $61.5^{+8.4}_{-7.8}$ mÅ or equivalently $3.93^{+0.54}_{-0.50}$ % in absorption depth over their observing baseline of ∼1.5 years. Over a three week time scale, the difference between our transit observations and subsequent additional out-of-transit baseline for V1298 Tau, Krolikowski et al. (2024) measure variability of ∼80 mÅ, serving as

a cautionary tale against using out of transit data from different epochs for these young systems.

We also measure variability in the stellar helium line between our December and January out-of-transit observations. Over this 3 week time scale, the helium equivalent width varied from 453.784 mÅ to 418.649 mÅ (integrated between 10831.58 Å and 10835.48 Å). The equivalent widths and variability are similar to that seen by Krolikowski et al. (2024). We were motivated to use the January out-of-transit spectra because we were only able to acquire three out-of-transit spectra immediately before the December transit due to poor weather. However, in doing so, we are insensitive to planetary absorption because of the large amplitude variability in the stellar helium line. For this reason, we recalculated V1298 Tau c's transmission spectrum using only the December out-of-transit data. This approach also reveals no in-transit He absorption with an upper limit of 0.55 %, which is consistent with our original approach of using the January data, and hence does not change our conclusions.

5.2. *Young Planets in Context*

To contextualize the helium non-detections presented here for K2-100b, HD 63433b, and V1298 Tau c, we compare our derived He upper limits to measured helium equivalent widths from the literature for sub-Jovian ($R_\oplus \leq 6$) planets orbiting K dwarfs and other stellar host types in Figure 14. We also compare these helium measurements to 1D hydrodynamic modeling predictions with planetary evolution. We extend upon the work of Allan et al. (2024), by computing two new self-consistent model sets better suited to the three planets discussed in this work, namely a smaller $0.1\,M_J$ planet orbiting the same K-type star at 0.045 au, again considering both 2% and 10% He abundances. For the radius evolution input, we use the models of Fortney & Nettelmann (2010) for a $0.1\,M_J$ planet, with a $25\,M_\oplus$ planetary core. Over the considered evolution timeframe of 16 to 5000 Myr, the radius evolves from 0.83 to $0.55\,R_J$, closer to – but still above – the radii of the planets here (0.346, 0.192, 0.499 and R_J for K2-100b, HD 63433b, and V1298 Tau c, respectively). Other than these smaller radius and mass inputs, the modeling of the evolution predictions presented here is identical to the F2 and F10 model sets of Allan et al. (2024).

Compared to these previous larger, inflated models, the two new self-consistent evolution model sets experience a stronger gravitational force due to the smaller planetary radius (despite the lower planetary mass assumed). Consequently, the predicted atmospheric escape is also lower. During transit, this, in addition to

the smaller planetary radii results in relatively reduced coverage of the stellar disk by atmospheric triplet-state helium and ultimately a lower predicted observability of escape. However, the overall trend of weaker He absorption with evolution noted in Allan et al. (2024) remains in the new $0.1\,M_J$ model-sets, with the solid and dashed profiles of Figure 14 corresponding to 2% and 10% He abundances.

Considering the non-detections we find here and the high estimated mass-loss rates from both our hydrodynamic escape models (isothermal Parker wind and photoevaporation-driven escape), we consider the ages of the systems in our sample and the timescales of photoevaporation assuming a constant mass-loss rate with evolution. For HD 63433 b, the self-consistent model's predicted mass-loss rate of $2.8 \times 10^{10}\,\mathrm{g\,s^{-1}}$ gives an evaporation timescale of 215 Myr if we adopt the same envelope fraction of 0.6% (Zhang et al. 2022c). This rough estimation is also likely underestimated due to our assumption of a constant mass-loss rate with evolution, due to the escape likely being stronger at ages younger than the sampled age in reality. Given HD 63433 b's predicted age (414±23 Myr; Mann et al. 2020), both p-winds and our hydrodynamic models are consistent with (Zhang et al. 2022b) in demonstrating that it is unlikely that the planet has retained a H/He atmosphere.

Applying the constant mass loss with evolution approximation to V1298 Tau c and K2-100 b results in photoevaporation timescales of 140 and 225 Myr, respectively. Using a more ample envelope fraction of 2% for mini-Neptunes leads to timescales of 465 and 740 Myr. Regardless of the assumed envelope fraction, the very expected young age of V1298 Tau c ($23 \pm 4\,\mathrm{Myr}$) suggests that it should still have its primordial atmosphere. K2-100b – with its age of $750 \pm 5\,\mathrm{Myr}$ – may be close to its photoevaporation lifetime, depending on the mass fraction of the envelope. Furthermore, the hydrodynamic modeling (which assumes a primordial atmosphere) shows that the loss of the primordial atmosphere is not required to explain the non-detections – the low number density of helium triplet material obscuring the disk alone is enough to do so.

We therefore propose three different explanations for the He non-detections presented here: i) it is possible that the planets formed with a low He abundance; ii) stellar winds and/or magnetic field effects quash the He signal (§4.1); or iii) escape is occurring, but helium is not in the metastable state (§4.3) and thus not observable with our $1.083\,\mu m$ data. Magnetic fields are consistent with the HD 63433b non-detection, while the K2-100 and V1298 Tau c non-detections do not require magnetic fields and can instead be explained by a combination of

the Hill radii and likely optically thin nature of He being less than our detection threshold, combined with some potential stellar wind confinement.

Intriguingly, the majority of previously published He I observations for young sub-Jovian planets have yielded several non-detections (e.g., Gaidos et al. 2020; Vissapragada et al. 2021; Zhang et al. 2022c, 2023) – contrary to theoretical predictions of higher or ongoing atmospheric escape rates early on in the evolutionary timescales of these systems. Long-term monitoring of stellar helium variability for a sample of mostly young stars (Krolikowski et al. 2024) – including the three planets that are the subject of this study – show that exoplanet helium absorption is typically less than the stellar helium variability at ages < 300 Myr. This presents another confounding factor for better understanding young planets.

6. CONCLUSIONS

Using Keck II/NIRSPEC, we observed the helium transmission spectra for three young (<800 Myr) sub-Jovian (0.2–0.5 R_J) planets: HD 63433b, K2-100b, and V1298 Tau c. We find upper limits on the excess helium absorption ranging from 0.47–1.13% for all three planets in this sample, with upper limits on their mass-loss rates of $7.9 \times 10^{10} - 7.9 \times 10^{11}\,\mathrm{g\,s^{-1}}$ from Parker wind models (§4.2). These observed upper limits are consistent with the analytical maximum excess absorption predictions at $1.083\,\mu$m ($\sim$2–8%; §4.1) and estimates of <0.04–0.6% from 1D hydrodynamic escape models (§4.3). In the context of other He observations of sub-Jovian planets in both young and older systems, our results follow theoretical predictions for the exponential decay of helium absorption in sub-Jovians as a function of system age. Further $1.083\,\mu$m observations for a larger sample of sub-Jovian planets at a range of ages is crucial for better understanding the temporal evolution of the helium triplet.

REFERENCES

Adams, F. C. 2011, ApJ, 730, 27,
doi: 10.1088/0004-637X/730/1/27

Allan, A., & Vidotto, A. A. 2019, MNRAS, 490, 3760,
doi: 10.1093/mnras/stz2842

Allan, A. P., Vidotto, A. A., Villarreal D'Angelo, C., Dos Santos, L. A., & Driessen, F. A. 2024, MNRAS, 527, 4657, doi: 10.1093/mnras/stad3432

Allart, R., Bourrier, V., Lovis, C., et al. 2018, Science, 362, 1384, doi: 10.1126/science.aat5879

Alonso-Floriano, F. J., Snellen, I. A. G., Czesla, S., et al. 2019, A&A, 629, A110,
doi: 10.1051/0004-6361/201935979

Barragán, O., Aigrain, S., Kubyshkina, D., et al. 2019, MNRAS, 490, 698, doi: 10.1093/mnras/stz2569

Batalha, N. M., Rowe, J. F., Bryson, S. T., et al. 2013, ApJS, 204, 24, doi: 10.1088/0067-0049/204/2/24

Bellotti, S., Morin, J., Lehmann, L. T., et al. 2024, arXiv e-prints, arXiv:2403.08590,
doi: 10.48550/arXiv.2403.08590

Ben-Jaffel, L., Ballester, G. E., García Muñoz, A., et al. 2022, Nature Astronomy, 6, 141,
doi: 10.1038/s41550-021-01505-x

Biassoni, F., Caldiroli, A., Gallo, E., et al. 2023, arXiv e-prints, arXiv:2310.13052,
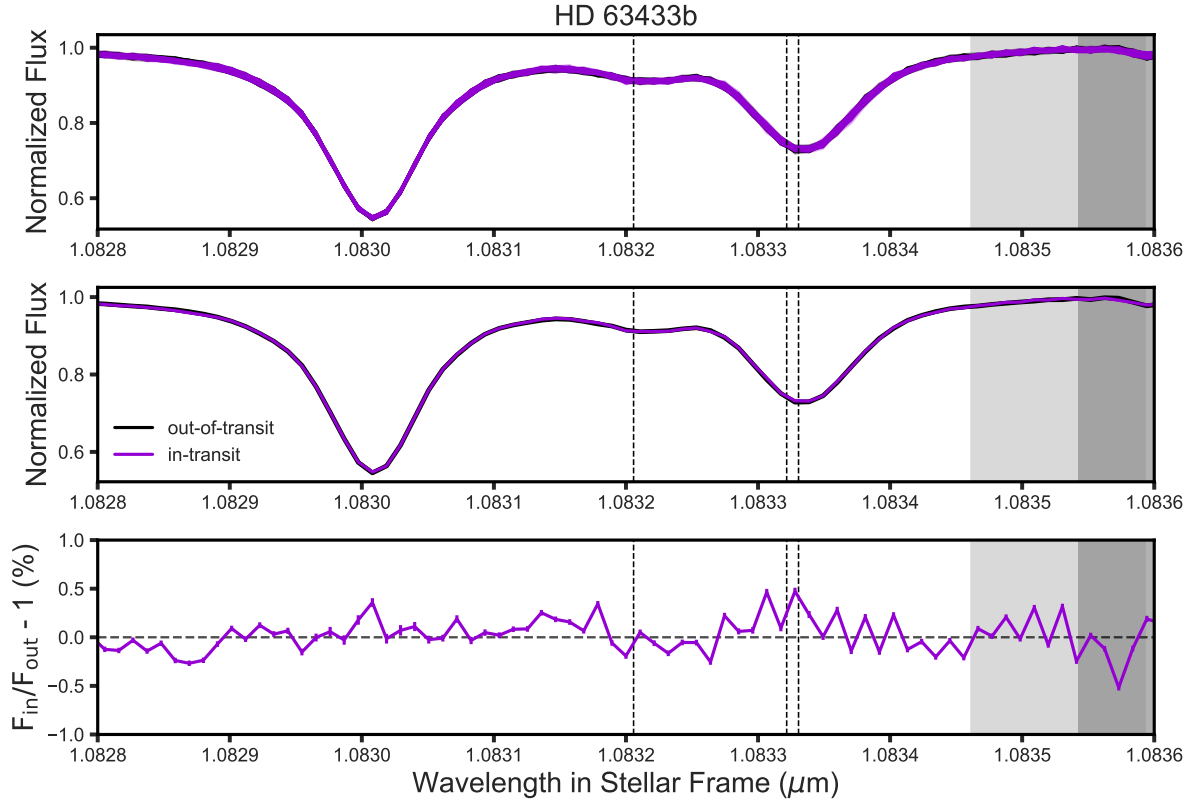doi: 10.48550/arXiv.2310.13052
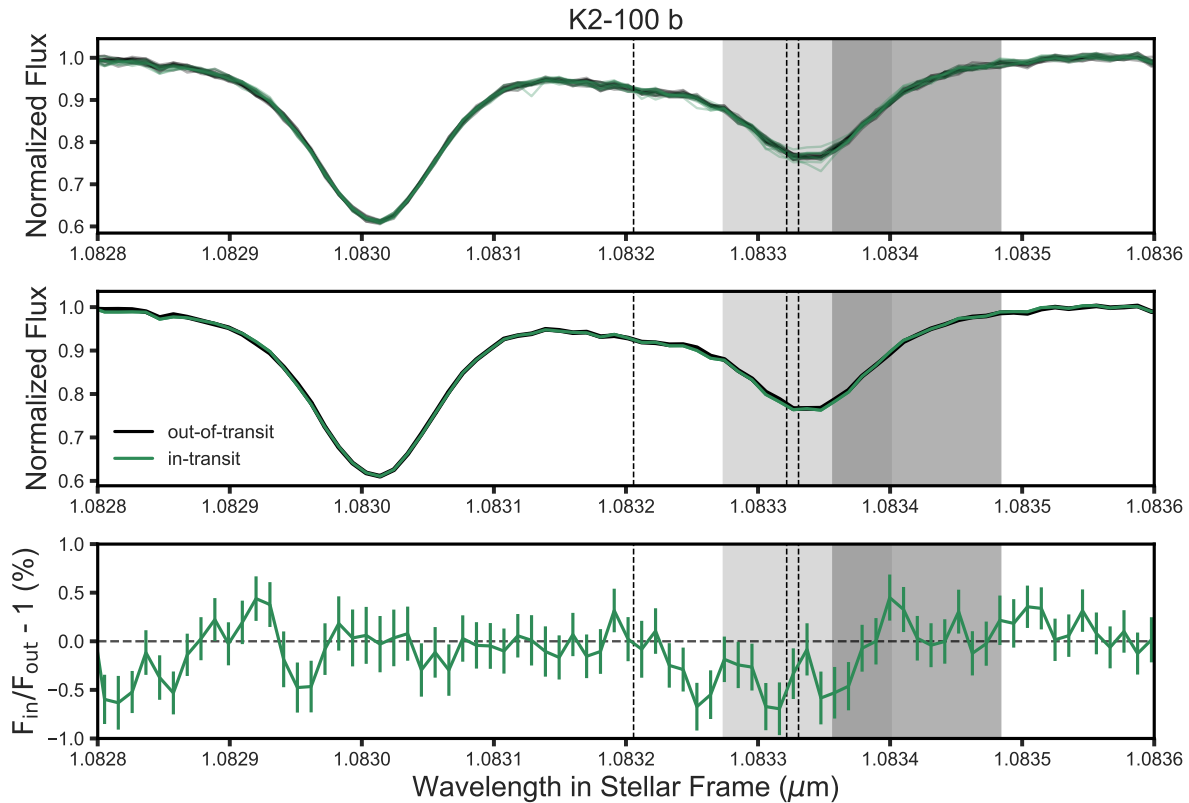
Figure 2. In-transit (green) and out-of-transit (black) stellar spectra of K2-100b for all individual spectral frames (top) and the mean spectra (middle), as well as the excess absorption (bottom) centered on the helium triplet (dashed black lines). The OH emission (light gray) and H_2O absorption (dark gray) telluric regions are also indicated.

Blackman, E. G., & Owen, J. E. 2016, MNRAS, 458, 1548, doi: 10.1093/mnras/stw369

Blanco-Cuaresma, S. 2019, MNRAS, 486, 2075, doi: 10.1093/mnras/stz549

Blanco-Cuaresma, S., Soubiran, C., Heiter, U., & Jofré, P. 2014, A&A, 569, A111, doi: 10.1051/0004-6361/201423945

Bourrier, V., Ehrenreich, D., & Lecavelier des Etangs, A. 2015, A&A, 582, A65, doi: 10.1051/0004-6361/201526894

Bourrier, V., & Lecavelier des Etangs, A. 2013, A&A, 557, A124, doi: 10.1051/0004-6361/201321551

Bourrier, V., Ehrenreich, D., Wheatley, P. J., et al. 2017, A&A, 599, L3, doi: 10.1051/0004-6361/201630238

Bourrier, V., Lecavelier des Etangs, A., Ehrenreich, D., et al. 2018, A&A, 620, A147, doi: 10.1051/0004-6361/201833675

Brandt, T. D., & Huang, C. X. 2015, ApJ, 807, 58, doi: 10.1088/0004-637X/807/1/58

Capistrant, B. K., Soares-Furtado, M., Vanderburg, A., et al. 2024, AJ, 167, 54, doi: 10.3847/1538-3881/ad1039

Carolan, S., Vidotto, A. A., Plavchan, P., Villarreal D'Angelo, C., & Hazra, G. 2020, MNRAS, 498, L53, doi: 10.1093/mnrasl/slaa127

Chen, J., & Kipping, D. 2017, ApJ, 834, 17, doi: 10.3847/1538-4357/834/1/17

David, T. J., Petigura, E. A., Luger, R., et al. 2019, ApJL, 885, L12, doi: 10.3847/2041-8213/ab4c99

Dos Santos, L. A., & Vissapragada, S. 2023, p-winds, v1.4.4, Zenodo, doi: 10.5281/zenodo.7814782

Dos Santos, L. A., Ehrenreich, D., Bourrier, V., et al. 2020, A&A, 634, L4, doi: 10.1051/0004-6361/201937327

Dos Santos, L. A., Vidotto, A. A., Vissapragada, S., et al. 2022, A&A, 659, A62, doi: 10.1051/0004-6361/202142038

Dressing, C. D., & Charbonneau, D. 2015, ApJ, 807, 45, doi: 10.1088/0004-637X/807/1/45

Duvvuri, G. M., Cauley, P. W., Aguirre, F. C., et al. 2023, AJ, 166, 196, doi: 10.3847/1538-3881/acfa74

Ehrenreich, D., Bourrier, V., Wheatley, P. J., et al. 2015, Nature, 522, 459, doi: 10.1038/nature14501

Figure 3. In-transit (purple) and out-of-transit (black) stellar spectra of HD 63433b for all spectral frames (top) and the mean spectra (middle), as well as the excess absorption (bottom) centered on the helium triplet (dashed black lines). The OH emission (light gray) and H_2O absorption (dark gray) telluric regions are also indicated.

Feinstein, A. D., David, T. J., Montet, B. T., et al. 2022, ApJL, 925, L2, doi: 10.3847/2041-8213/ac4745

Feinstein, A. D., Montet, B. T., Johnson, M. C., et al. 2021, AJ, 162, 213, doi: 10.3847/1538-3881/ac1f24

Foreman-Mackey, D., Agol, E., Ambikasaran, S., & Angus, R. 2017, AJ, 154, 220, doi: 10.3847/1538-3881/aa9332

Fortney, J. J., & Nettelmann, N. 2010, Space Science Reviews, 152, 423, doi: 10.1007/s11214-009-9582-x

Fulton, B. J., Petigura, E. A., Howard, A. W., et al. 2017, AJ, 154, 109, doi: 10.3847/1538-3881/aa80eb

Gaidos, E., Hirano, T., Mann, A. W., et al. 2020, MNRAS, 495, 650, doi: 10.1093/mnras/staa918

Gaidos, E., Hirano, T., Beichman, C., et al. 2022, MNRAS, 509, 2969, doi: 10.1093/mnras/stab3107

Gaidos, E., Hirano, T., Lee, R. A., et al. 2023, MNRAS, 518, 3777, doi: 10.1093/mnras/stac3301

Ginzburg, S., Schlichting, H. E., & Sari, R. 2018, MNRAS, 476, 759, doi: 10.1093/mnras/sty290

Guilluy, G., Bourrier, V., Jaziri, Y., et al. 2023, A&A, 676, A130, doi: 10.1051/0004-6361/202346419

Husser, T. O., Wende-von Berg, S., Dreizler, S., et al. 2013, A&A, 553, A6, doi: 10.1051/0004-6361/201219058

Jackson, A. P., Davis, T. A., & Wheatley, P. J. 2012, MNRAS, 422, 2024, doi: 10.1111/j.1365-2966.2012.20657.x

Johnstone, C. P., Güdel, M., Brott, I., & Lüftinger, T. 2015, A&A, 577, A28, doi: 10.1051/0004-6361/201425301

Jones, J., White, R. J., Boyajian, T., et al. 2015, ApJ, 813, 58, doi: 10.1088/0004-637X/813/1/58

Kasper, D., Bean, J. L., Oklopčić, A., et al. 2020, AJ, 160, 258, doi: 10.3847/1538-3881/abbee6

Kausch, W., Noll, S., Smette, A., et al. 2015, A&A, 576, A78, doi: 10.1051/0004-6361/201423909

Kirk, J., Alam, M. K., López-Morales, M., & Zeng, L. 2020, AJ, 159, 115, doi: 10.3847/1538-3881/ab6e66

Kirk, J., Dos Santos, L. A., López-Morales, M., et al. 2022, arXiv e-prints, arXiv:2205.11579. https://arxiv.org/abs/2205.11579

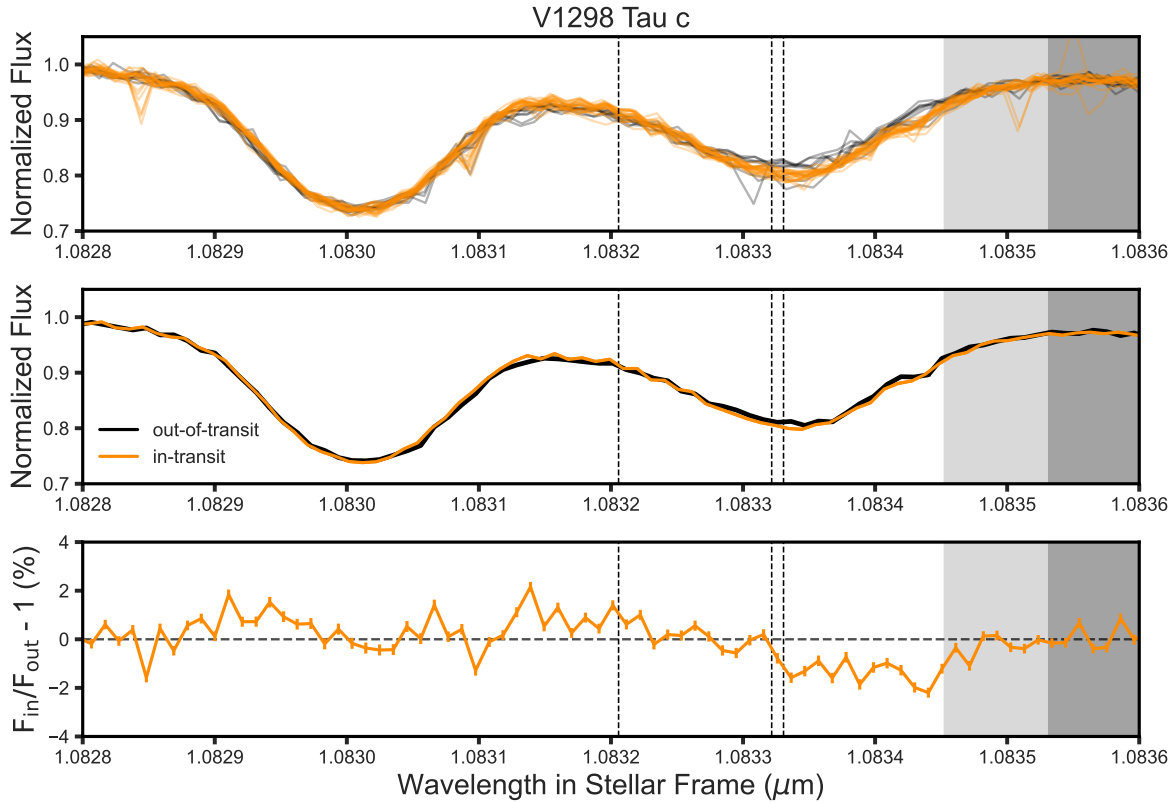Klein, B., Zicher, N., Kavanagh, R. D., et al. 2022a, MNRAS, 512, 5067, doi: 10.1093/mnras/stac761

Figure 4. In-transit (orange) and out-of-transit (black) stellar spectra of V1298 Tau c for all spectral frames (top) and the mean spectra (middle), as well as the excess absorption (bottom) centered on the helium triplet (dashed black lines). The OH emission (light gray) and H_2O absorption (dark gray) telluric regions are also indicated.

—. 2022b, MNRAS, 512, 5067, doi: 10.1093/mnras/stac761

Krishnamurthy, V., Hirano, T., Stefánsson, G., et al. 2021, AJ, 162, 82, doi: 10.3847/1538-3881/ac0d57

Krolikowski, D. M., Kraus, A. L., Tofflemire, B. M., et al. 2024, AJ, 167, 79, doi: 10.3847/1538-3881/ad0f22

Lammer, H. 2013, Origin and Evolution of Planetary Atmospheres, doi: 10.1007/978-3-642-32087-3

Lampón, M., López-Puertas, M., Lara, L. M., et al. 2020, A&A, 636, A13, doi: 10.1051/0004-6361/201937175

Lecavelier Des Etangs, A. 2007, A&A, 461, 1185, doi: 10.1051/0004-6361:20065014

Lecavelier Des Etangs, A., Ehrenreich, D., Vidal-Madjar, A., et al. 2010, A&A, 514, A72, doi: 10.1051/0004-6361/200913347

Livingston, J. H., Dai, F., Hirano, T., et al. 2018, AJ, 155, 115, doi: 10.3847/1538-3881/aaa841

Lopez, E. D., & Fortney, J. J. 2014, ApJ, 792, 1, doi: 10.1088/0004-637X/792/1/1

Lopez, E. D., Fortney, J. J., & Miller, N. 2012, ApJ, 761, 59, doi: 10.1088/0004-637X/761/1/59

Loyd, R. O. P., France, K., Youngblood, A., et al. 2018, ApJ, 867, 71, doi: 10.3847/1538-4357/aae2bd

MacLeod, M., & Oklopčić, A. 2022, ApJ, 926, 226, doi: 10.3847/1538-4357/ac46ce

Mann, A. W., Johnson, M. C., Vanderburg, A., et al. 2020, AJ, 160, 179, doi: 10.3847/1538-3881/abae64

Mansfield, M., Bean, J. L., Oklopčić, A., et al. 2018, ApJL, 868, L34, doi: 10.3847/2041-8213/aaf166

Martin, E. C., Fitzgerald, M. P., McLean, I. S., et al. 2018, in Society of Photo-Optical Instrumentation Engineers (SPIE) Conference Series, Vol. 10702, Ground-based and Airborne Instrumentation for Astronomy VII, ed. C. J. Evans, L. Simard, & H. Takami, 107020A, doi: 10.1117/12.2312266

McLean, I. S., McGovern, M. R., Burgasser, A. J., et al. 2003, ApJ, 596, 561, doi: 10.1086/377636

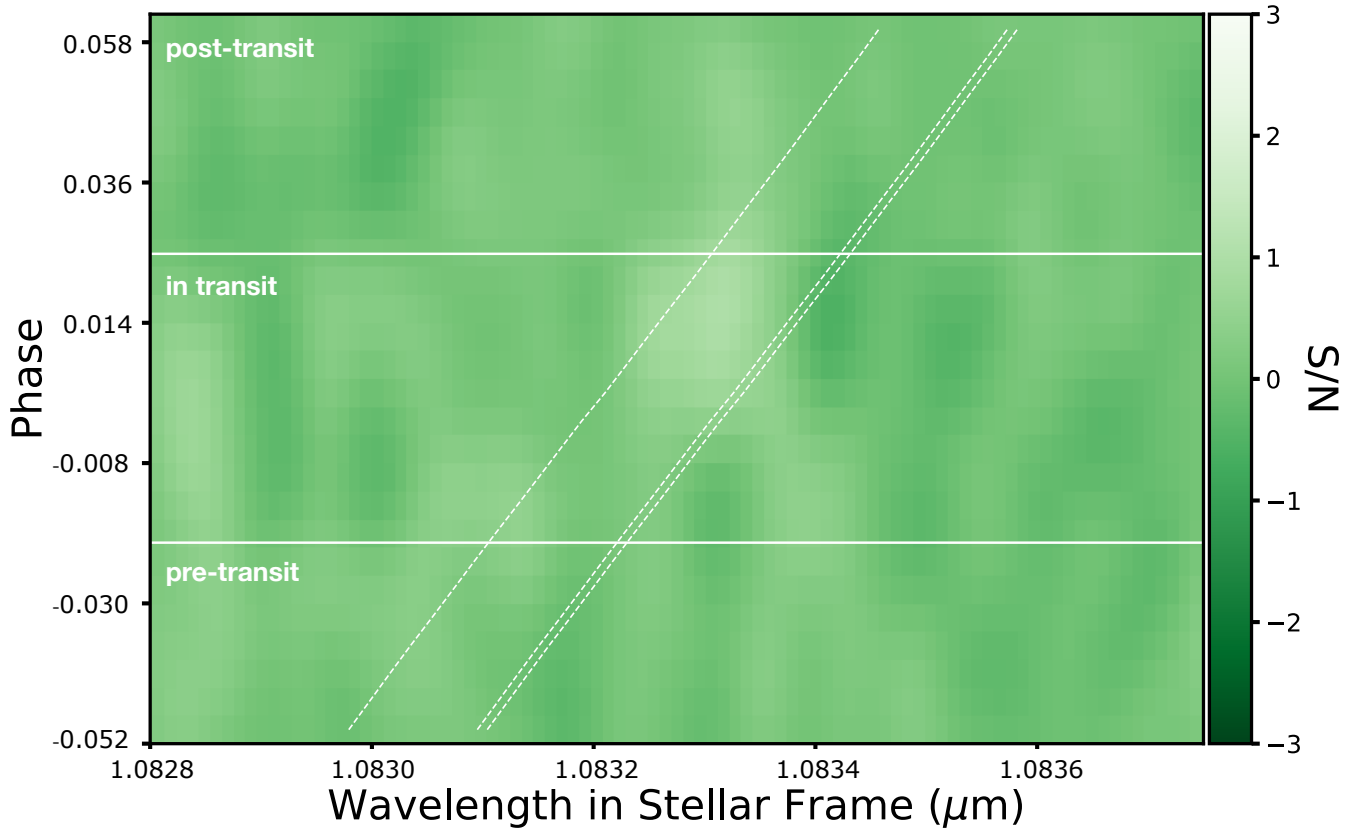McLean, I. S., Prato, L., McGovern, M. R., et al. 2007, ApJ, 658, 1217, doi: 10.1086/511740

Figure 5. Phase-resolved signal-to-noise map for K2-100b centered on the helium triplet in the stellar rest frame, compared to the first and fourth contact points (solid white lines) and the planet's orbital motion (dashed white lines).

McLean, I. S., Becklin, E. E., Bendiksen, O., et al. 1998, in Society of Photo-Optical Instrumentation Engineers (SPIE) Conference Series, Vol. 3354, Infrared Astronomical Instrumentation, ed. A. M. Fowler, 566–578, doi: 10.1117/12.317283

Morton, T. D., Bryson, S. T., Coughlin, J. L., et al. 2016, ApJ, 822, 86, doi: 10.3847/0004-637X/822/2/86

Murray-Clay, R. A., Chiang, E. I., & Murray, N. 2009, ApJ, 693, 23, doi: 10.1088/0004-637X/693/1/23

Nail, F., Oklopčić, A., & MacLeod, M. 2023, arXiv e-prints, arXiv:2312.04682, doi: 10.48550/arXiv.2312.04682

Nortmann, L., Pallé, E., Salz, M., et al. 2018, Science, 362, 1388, doi: 10.1126/science.aat5348

Oklopčić, A. 2019, ApJ, 881, 133, doi: 10.3847/1538-4357/ab2f7f

Oklopčić, A., & Hirata, C. M. 2018, ApJL, 855, L11, doi: 10.3847/2041-8213/aaada9

Orell-Miquel, J., Murgas, F., Pallé, E., et al. 2022, A&A, 659, A55, doi: 10.1051/0004-6361/202142455

Orell-Miquel, J., Lampón, M., López-Puertas, M., et al. 2023, A&A, 677, A56, doi: 10.1051/0004-6361/202346445

Owen, J. E., & Adams, F. C. 2014, MNRAS, 444, 3761, doi: 10.1093/mnras/stu1684

Owen, J. E., & Wu, Y. 2013, ApJ, 775, 105, doi: 10.1088/0004-637X/775/2/105

—. 2016, ApJ, 817, 107, doi: 10.3847/0004-637X/817/2/107

—. 2017, ApJ, 847, 29, doi: 10.3847/1538-4357/aa890a

Parker, E. N. 1958, Physical Review, 110, 1445, doi: 10.1103/PhysRev.110.1445

Rasmussen, C. E., & Williams, C. K. I. 2006, Gaussian Processes for Machine Learning (The MIT Press)

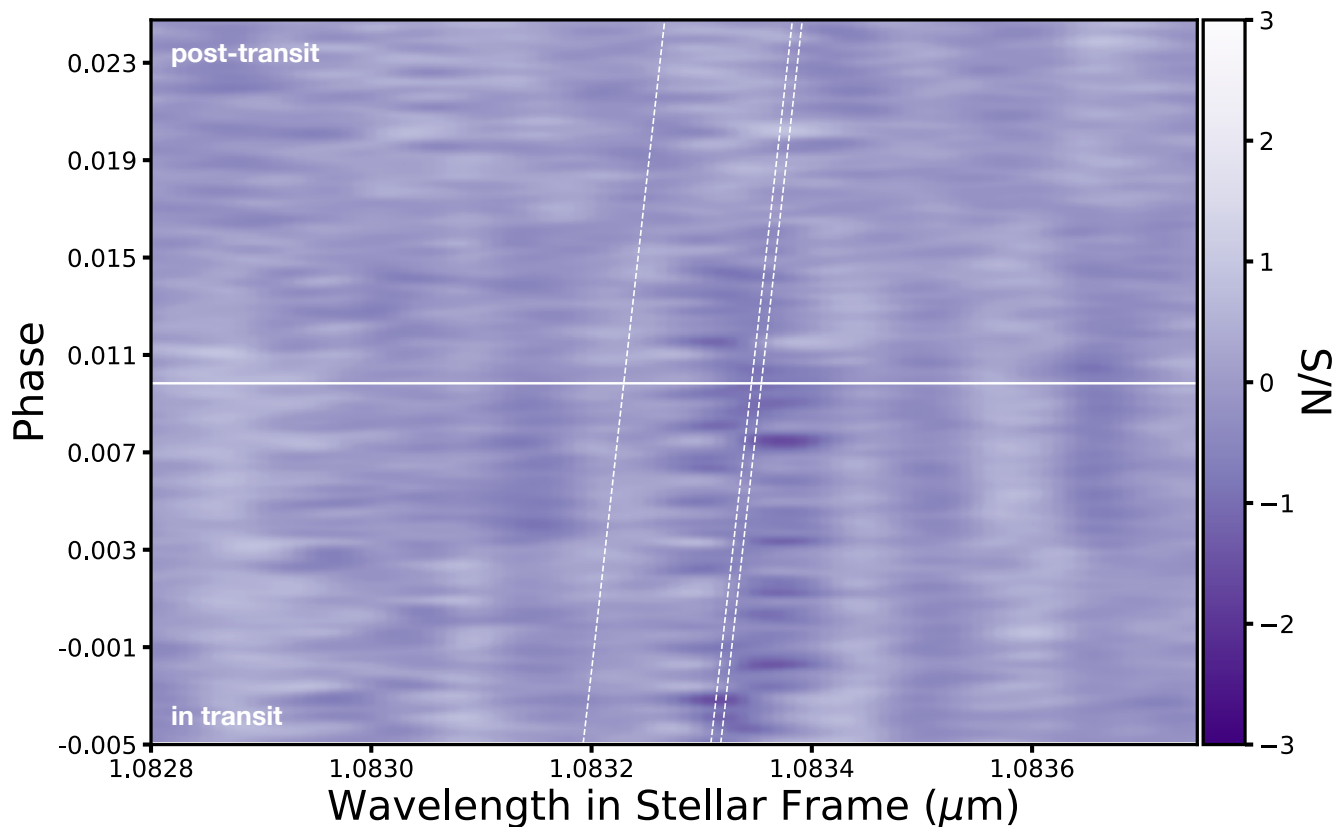Rogers, L. A. 2015, ApJ, 801, 41, doi: 10.1088/0004-637X/801/1/41

Figure 6. Phase-resolved signal-to-noise map of absorption for the partial transit (no pre-ingress baseline) of HD 63433b centered on the helium triplet in the stellar rest frame, compared to fourth contact (solid white line) and the planet's orbital motion (dashed white lines).

Sanz-Forcada, J., Stelzer, B., Coffaro, M., Raetz, S., & Alvarado-Gómez, J. D. 2019, A&A, 631, A45, doi: 10.1051/0004-6361/201935703

Schreyer, E., Owen, J. E., Spake, J. J., Bahroloom, Z., & Di Giampasquale, S. 2023, arXiv e-prints, arXiv:2302.10947. https://arxiv.org/abs/2302.10947

Seager, S., & Sasselov, D. D. 2000, ApJ, 537, 916, doi: 10.1086/309088

Smette, A., Sana, H., Noll, S., et al. 2015, A&A, 576, A77, doi: 10.1051/0004-6361/201423932

Spake, J. J., Sing, D. K., Evans, T. M., et al. 2018, Nature, 557, 68, doi: 10.1038/s41586-018-0067-5

Speagle, J. S. 2020, MNRAS, 493, 3132, doi: 10.1093/mnras/staa278

Stassun, K. G., Oelkers, R. J., Paegert, M., et al. 2019, AJ, 158, 138, doi: 10.3847/1538-3881/ab3467

Vidal-Madjar, A., Lecavelier des Etangs, A., Désert, J. M., et al. 2003, Nature, 422, 143, doi: 10.1038/nature01448

Vissapragada, S., Stefánsson, G., Greklek-McKeon, M., et al. 2021, AJ, 162, 222, doi: 10.3847/1538-3881/ac1bb0

Vissapragada, S., McCreery, P., Dos Santos, L. A., et al. 2024, ApJL, 962, L19, doi: 10.3847/2041-8213/ad23cf

Waalkes, W. C., Berta-Thompson, Z., Bourrier, V., et al. 2019, AJ, 158, 50, doi: 10.3847/1538-3881/ab24c2

Wood, B. E., Müller, H. R., Zank, G. P., Linsky, J. L., & Redfield, S. 2005, ApJL, 628, L143, doi: 10.1086/432716

Wright, J. T., & Eastman, J. D. 2014, PASP, 126, 838, doi: 10.1086/678541

Zhang, M., Knutson, H. A., Dai, F., et al. 2023, AJ, 165, 62, doi: 10.3847/1538-3881/aca75b

Zhang, M., Knutson, H. A., Wang, L., Dai, F., & Barragán, O. 2022a, AJ, 163, 67, doi: 10.3847/1538-3881/ac3fa7
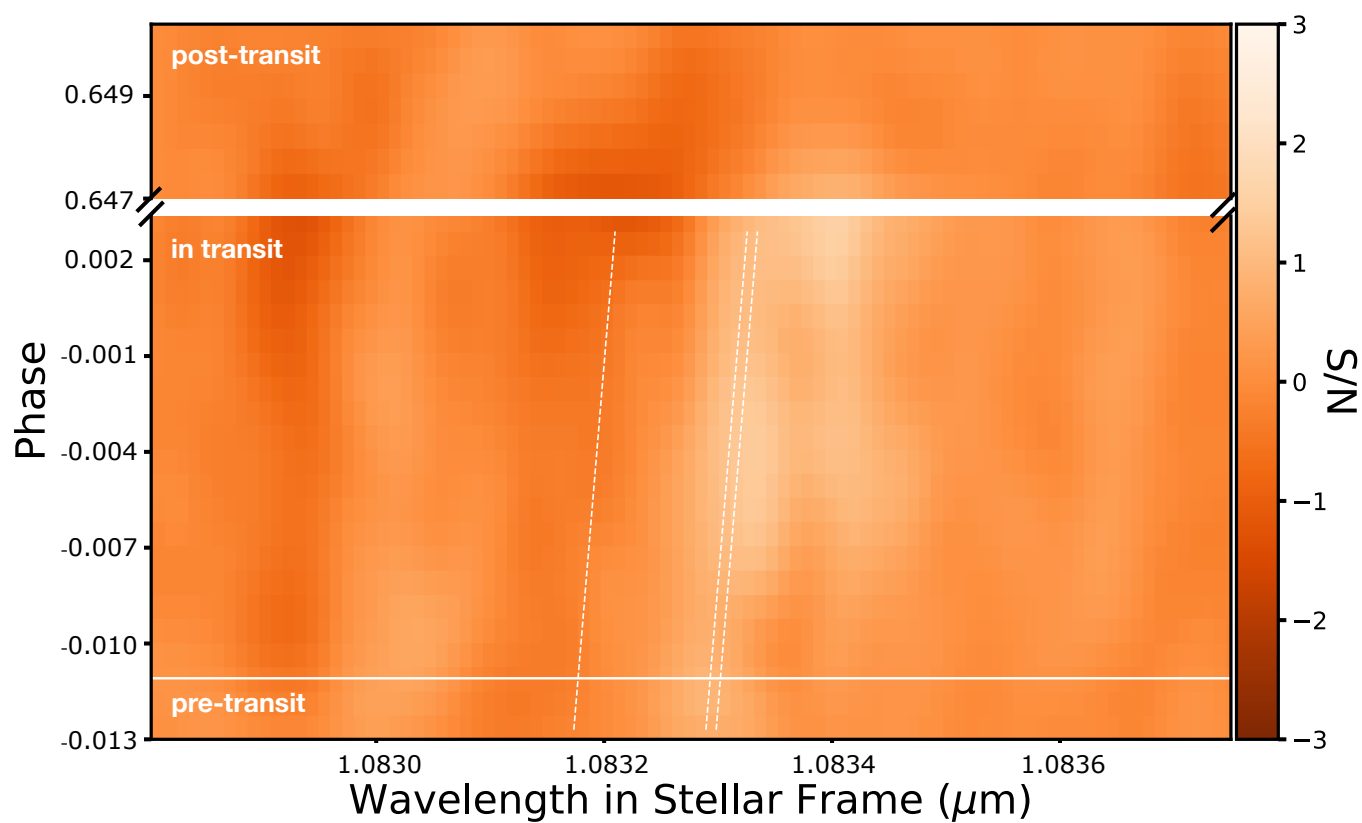
Figure 7. Phase-resolved signal-to-noise map for the partial transit of V1298 Tau c centered on the helium triplet in the stellar rest frame, compared to the first contact point (solid white lines) and the planet's orbital motion (dashed white lines).

Zhang, M., Knutson, H. A., Wang, L., et al. 2021, AJ, 161, 181, doi: 10.3847/1538-3881/abe382

—. 2022b, AJ, 163, 68, doi: 10.3847/1538-3881/ac3f3b

—. 2022c, AJ, 163, 68, doi: 10.3847/1538-3881/ac3f3b
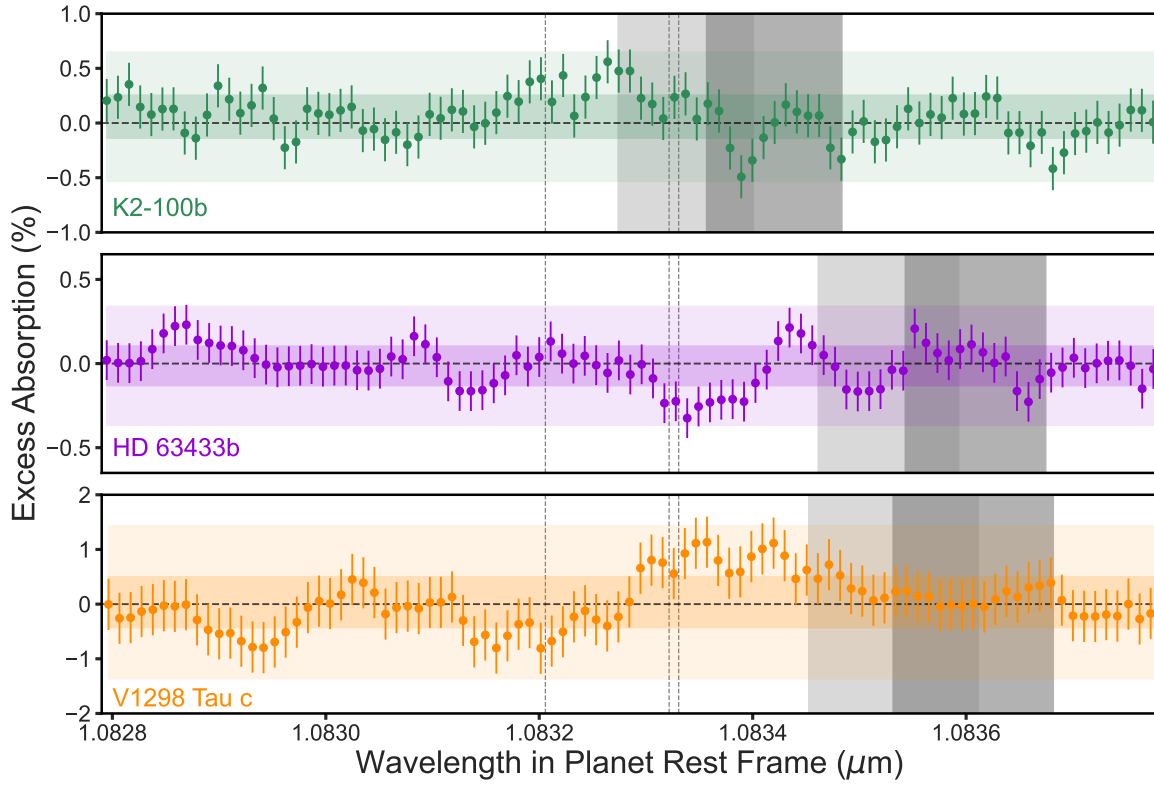
Figure 8. The He transmission spectrum for K2-100b (top), HD 63433b (middle), V1298 Tau c (bottom) centered on the helium triplet (dashed gray lines). The dark and light shaded colored regions correspond to the 1σ and 3σ uncertainties, respectively. Telluric regions are shown in the shaded gray regions, as in Figures 2, 3, and 4.
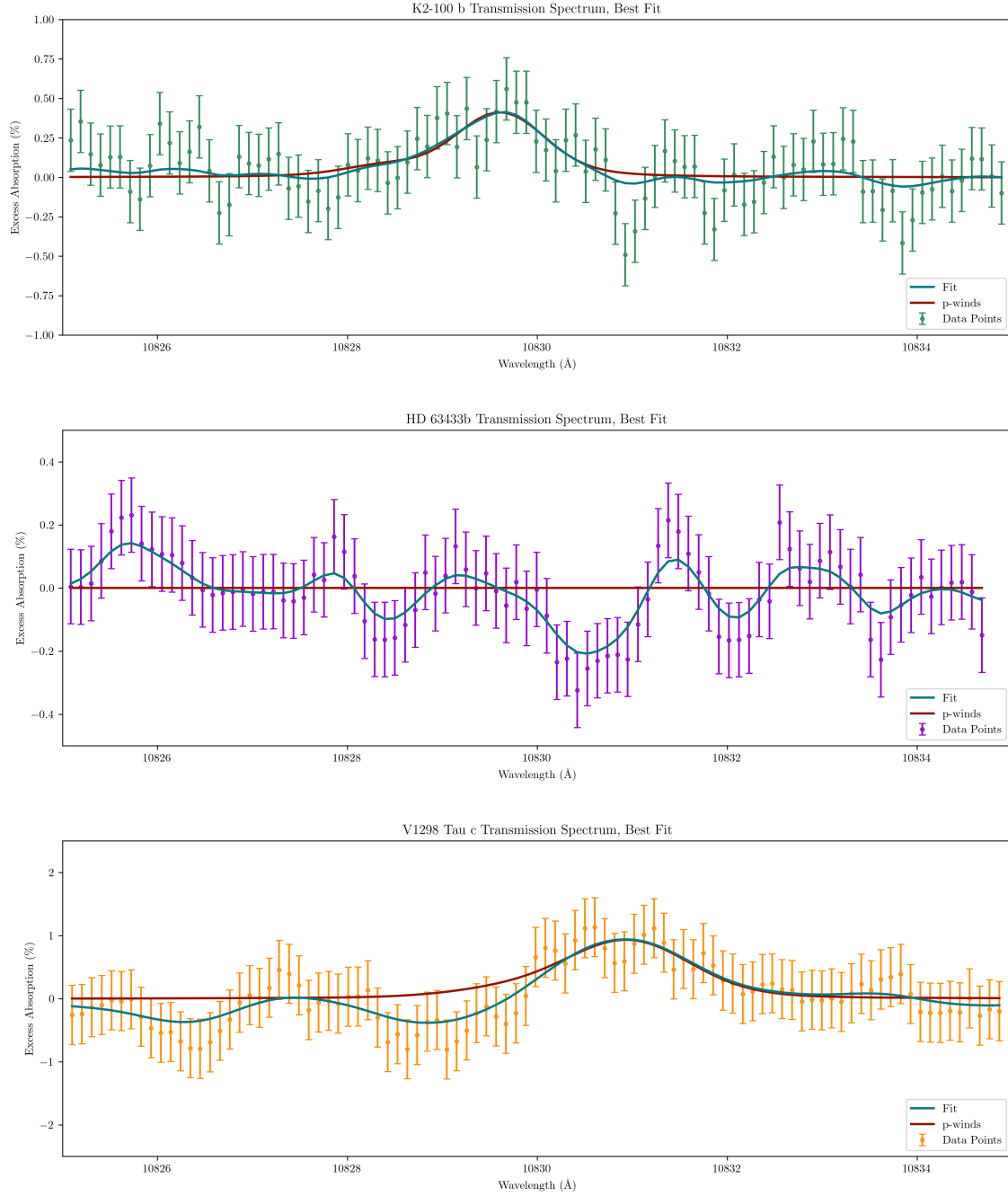
Figure 9. Best-fit results for simultaneously modeling the instrumental systematics and atmospheric escape signal.
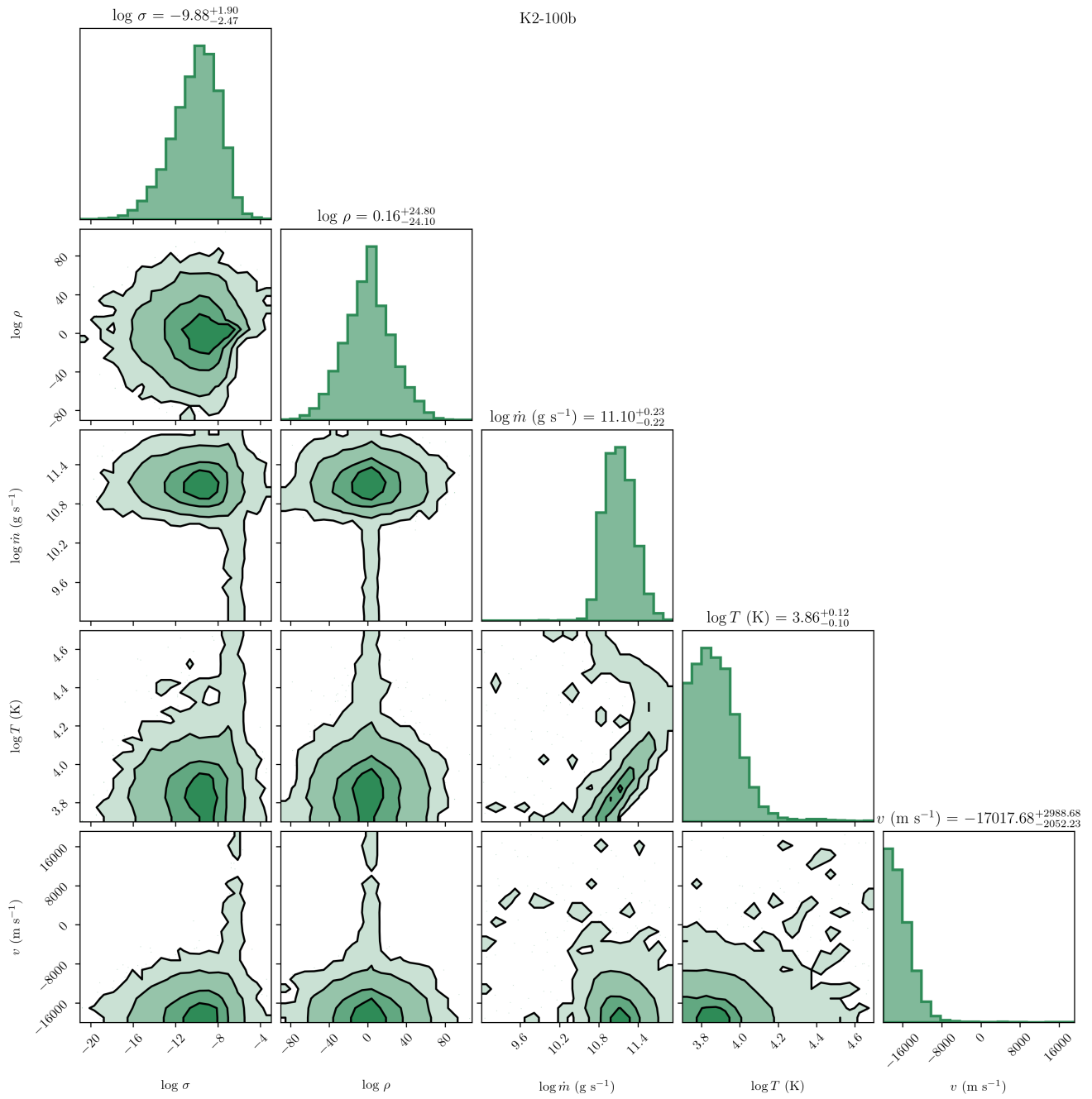
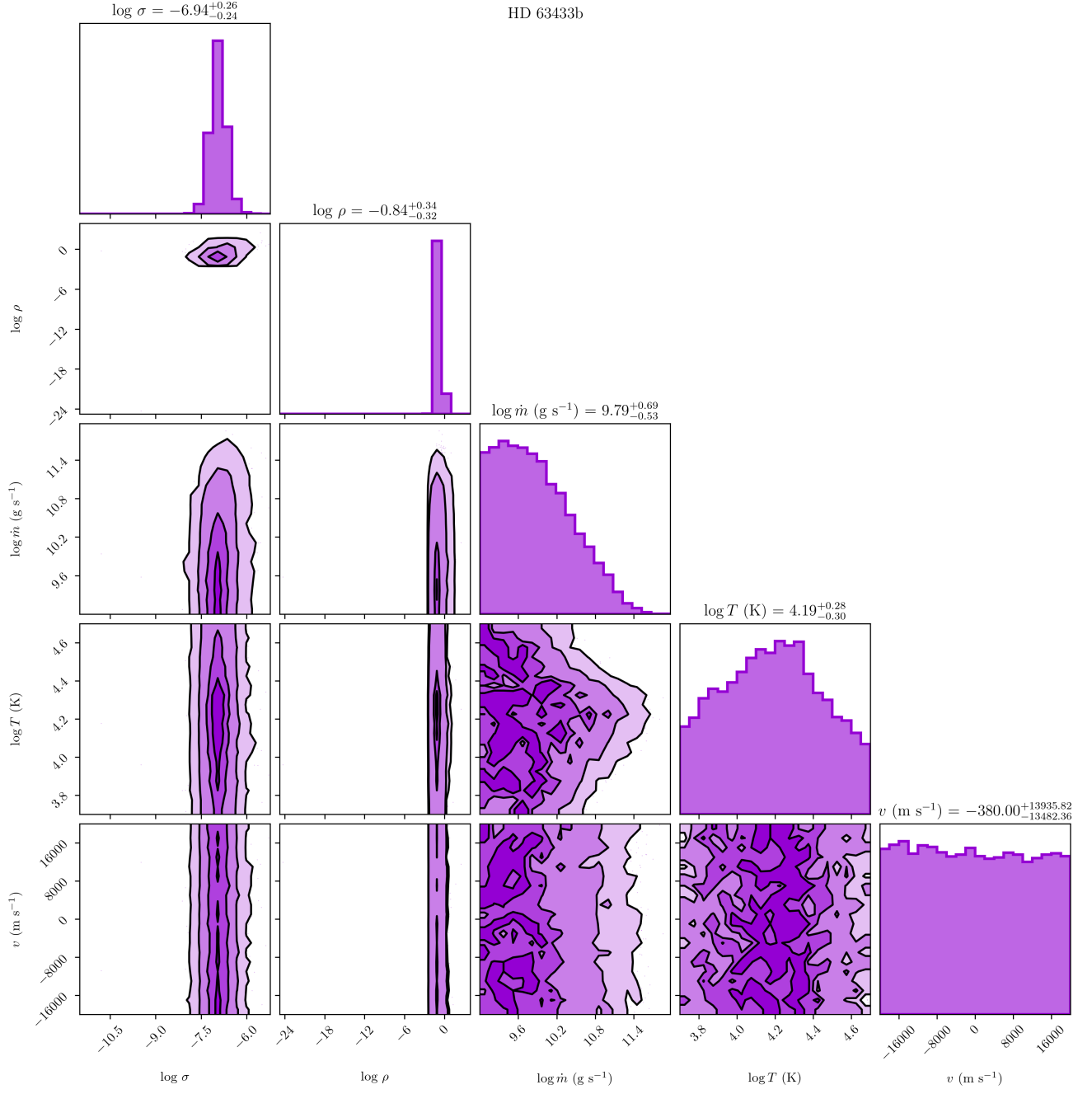**Figure 10.** Posterior distributions of retrieved parameters from our 1D `p-winds` models.

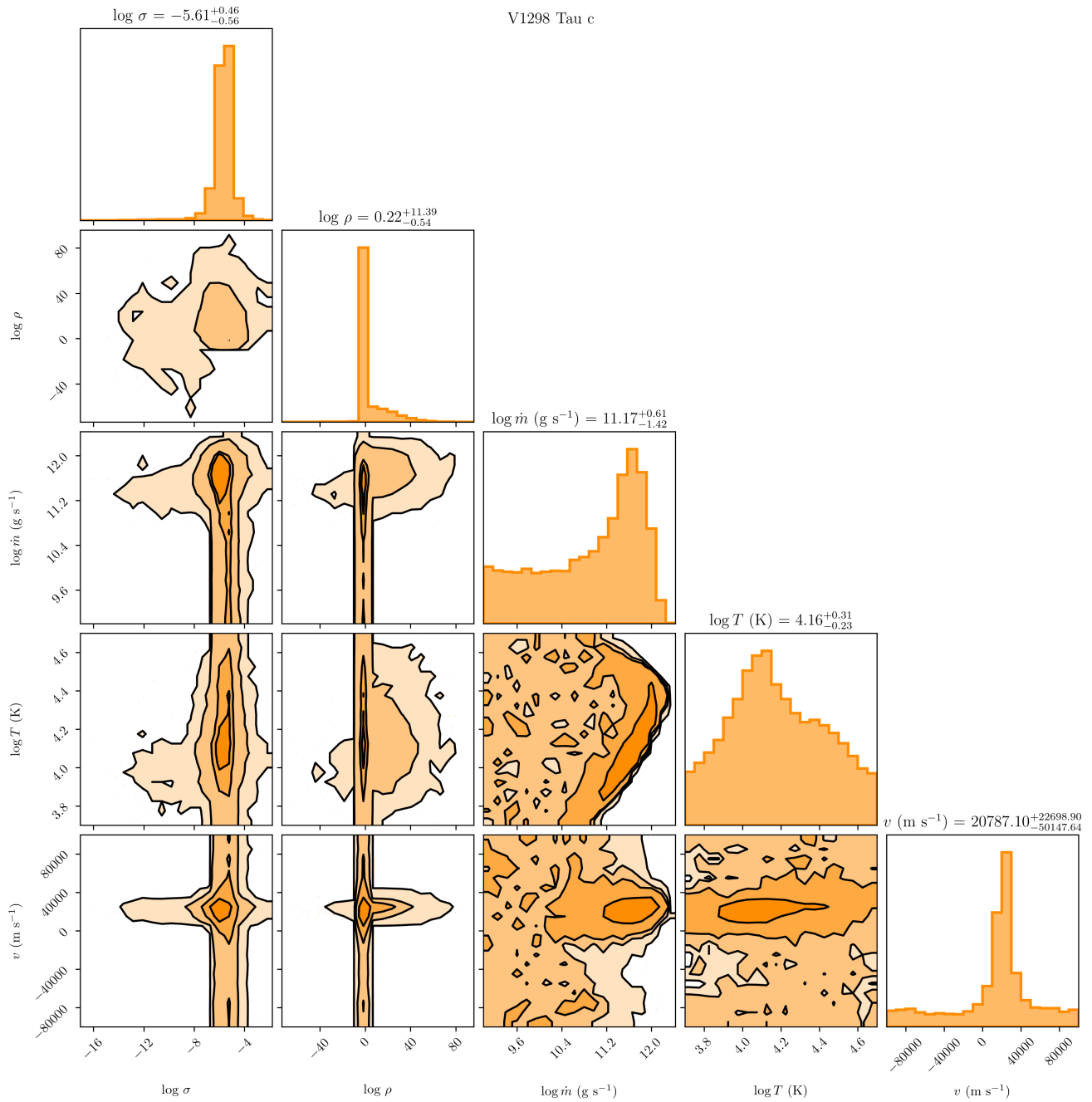**Figure 11.** Same as Figure 10, but for HD 63433b.

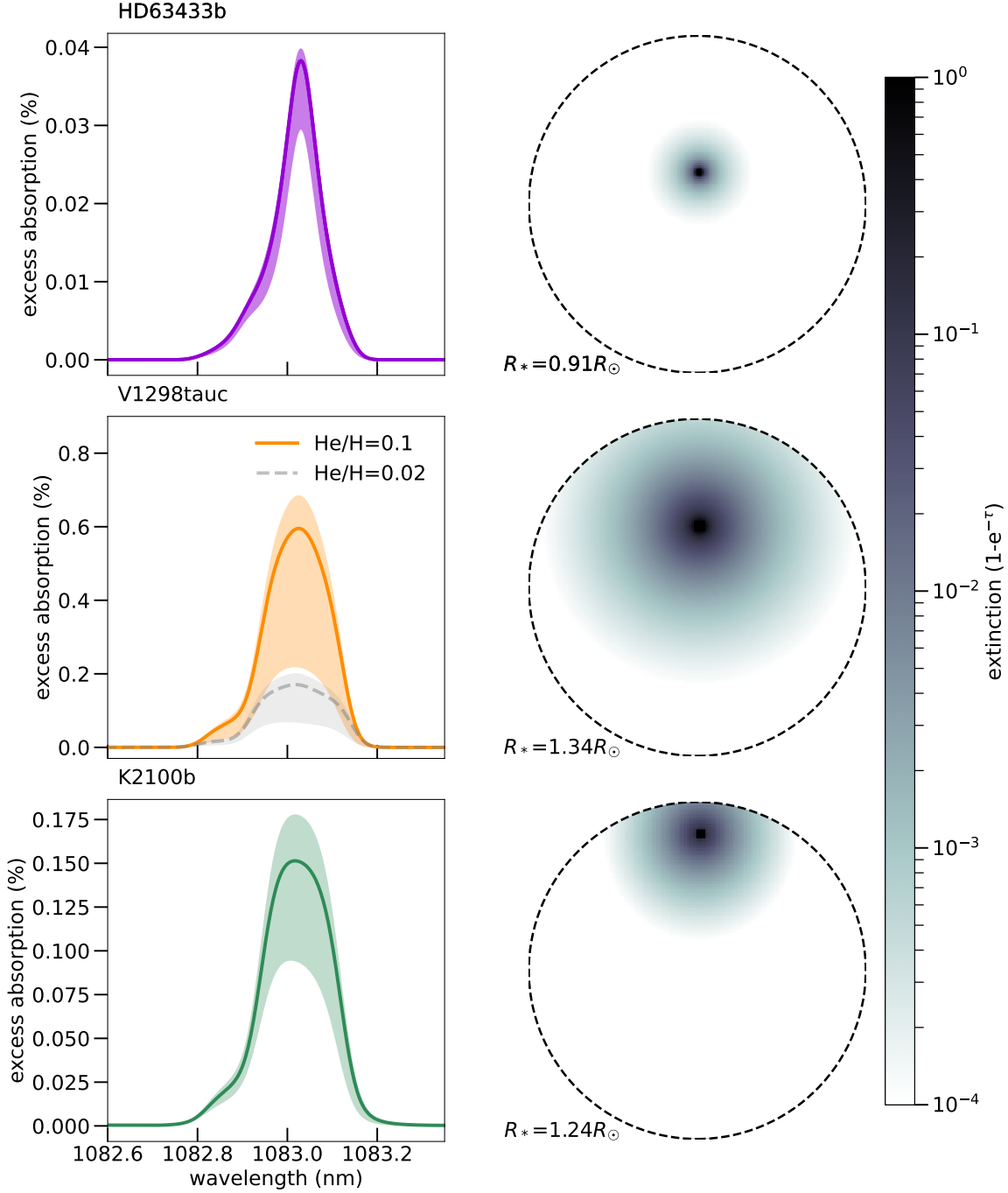**Figure 12.** Same as Figure 10, but for V1298 Tau c.

Figure 13. Helium triplet excess absorption predictions (left) and their corresponding mid-transit extinction maps (right), obtained with the model of Allan et al. (2024) as described in §4.3. For the excess absorption profiles, solid lines indicate mean phase averaged (T1-T4) profiles while shaded region encompasses all phases between first contact and mid-transit. For the extinction maps, the dashed circle marks the stellar disk. The displayed extinction is the sum of the three individual extinctions of each of the triplet lines. A helium to hydrogen number fraction of He/H=0.1 was assumed for each planet, with He/H=0.02 also being tested in the case of V1298 Tau c as shown by the gray dashed profile. Additional planetary and stellar parameters listed in Table 1 were used.
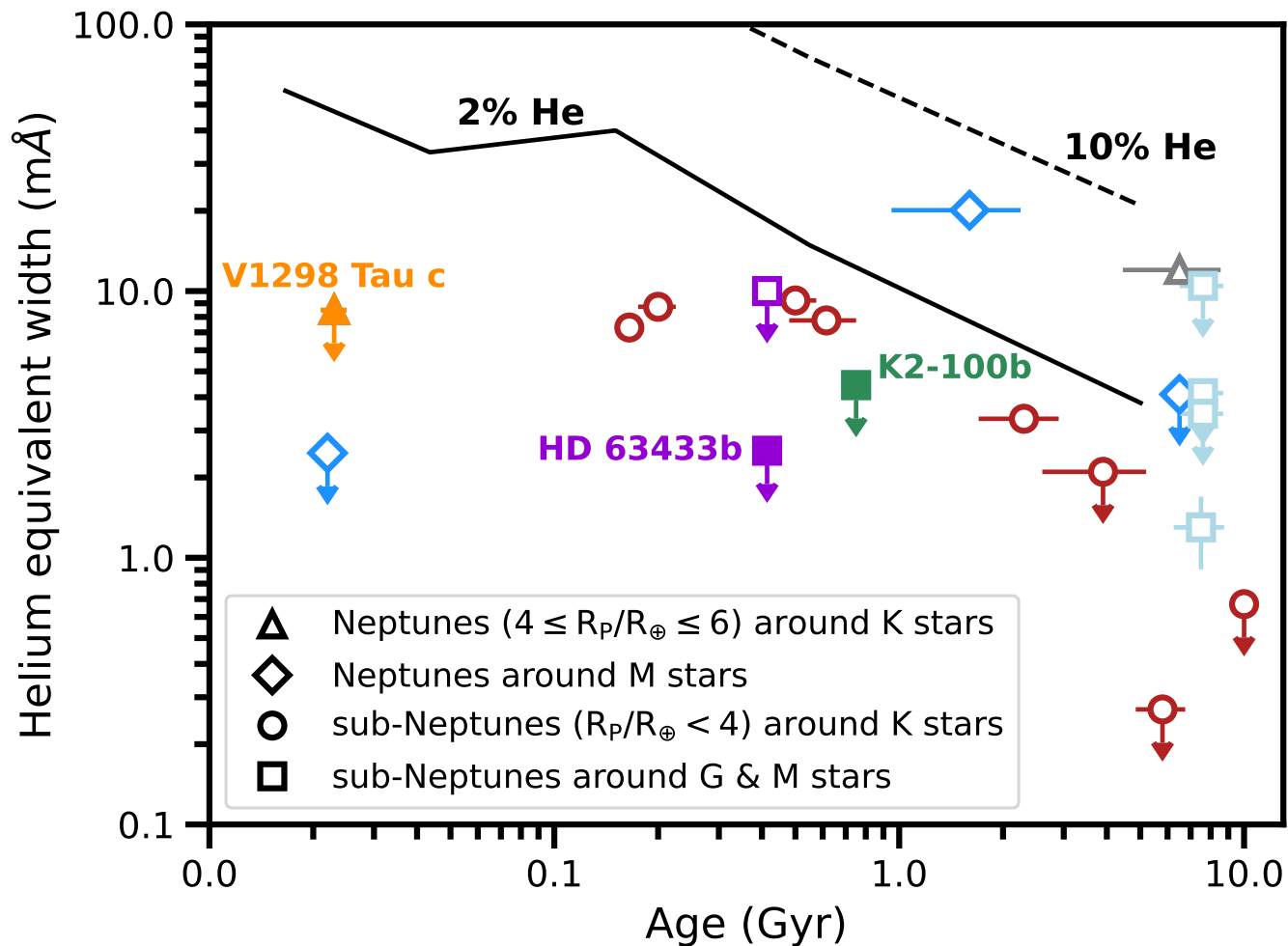
Figure 14. The measured equivalent width of the metastable helium line as a function of age for Neptunes ($4 \leq R_\oplus \leq 6$) around K stars (triangles) and M stars (diamonds), and sub-Neptunes ($R_\oplus < 4$) around K stars (circles) and around G and M stars (squares). The upper limits from our sample are shown for K2-100b (green), V1298 Tau c (orange), and HD 63433b (purple). The He equivalent width for HD 63433b from Zhang et al. (2022c) is shown in the open purple square. We also show predicted trends between helium absorption and age from hydrodynamic models (Allan et al. 2024) for 2% (solid black line) and 10% (dashed black line) He abundance. These models are calibrated for a $0.1\,\mathrm{M_{Jup}}$ planet orbiting a K-type star at $0.045\,\mathrm{au}$ (details in text). Literature helium values are taken from Allart et al. (2018); Gaidos et al. (2023); Kasper et al. (2020); Krishnamurthy et al. (2021); Nortmann et al. (2018); Orell-Miquel et al. (2022, 2023); Zhang et al. (2021, 2022a, 2023).